Wiley
Structural Control and Health Monitoring
Volume 2025, Article ID 1174744, 23 pages
https://doi.org/10.1155/stc/1174744

WILEY

Research Article

Shaking Table Real-Time Iterative Control Using Online System Matrix Correction

Ao Xun,[1,2] Hui-meng Zhou,[1,2] Zhen Wang,[3] Fu-rong Zhang,[4] Tao Wang,[5] Wei-xu Song,[6] David Wagg,[7] and Shuang Zou[1,2]

[1]*Engineering Seismic Research Center, Guangzhou University, Guangzhou 510006, China*
[2]*Guangdong Provincial Key Laboratory of Earthquake Engineering and Applied Technology, Guangzhou University, Guangzhou 510006, China*
[3]*School of Civil Engineering and Architecture, Wuhan University of Technology, Wuhan 430070, China*
[4]*Institute of Engineering Surveying and Mechanics Metrology, Yunnan Institute of Measuring and Testing Technology, Kunming 650228, China*
[5]*Key Laboratory of Earthquake Engineering and Engineering Vibration, Institute of Engineering Mechanics China Earthquake Administration, Harbin 150080, China*
[6]*Civil Engineering Structures Testing Department, BBK Test Systems Co. Ltd, Beijing 101102, China*
[7]*Department of Mechanical Engineering, The University of Sheffield, Sheffield S1 3JD, UK*

Correspondence should be addressed to Hui-meng Zhou; zhouhuimeng@gzhu.edu.cn and Zhen Wang; wang_zhen@whut.edu.cn

Received 5 November 2024; Revised 5 November 2025; Accepted 18 November 2025

Academic Editor: Lucia Faravelli

Offline iterative control (OIC) is a widely employed technique in shaking table tests for accurately reproducing earthquake waveforms. However, repeated offline iterations can cause cumulative damage to fragile specimens, while the continuously changing dynamic characteristics of nonlinear specimens reduce the control accuracy of OIC. To overcome these limitations, real-time iterative control (RIC) has been introduced and applied to eliminate the need for multiple iterations. To further improve the stability and accuracy of RIC, this study introduced RIC with online system matrix correction (RICSC) method, discussed the control performance of the RICSC method. The RICSC method evaluates the accuracy of the identified system matrix using the following indices: the coherence function (CF) weighted sum, the CF, and the autocorrelation power density spectrum (AS). Based on these evaluations, the system matrix is corrected via frame correction (FC) or frequency point (FP) correction algorithms, thereby enhancing waveform reproduction accuracy and control stability. The performance of the RICSC method was verified via numerical simulations and shaking table tests under 20 test conditions. The results show that the FP correction algorithm (RICSC-FP) achieves the fastest convergence of absolute error, and its reproduction accuracy is higher than those of the traditional RIC and FC (RICSC-FC) algorithms. Both numerical and experimental results demonstrate that the RICSC method provides higher reproduction accuracy than OIC after just one iteration.

Keywords: matrix accuracy evaluation indices; real-time iterative control; shaking table test; system matrix; system matrix correction algorithm

1. Introduction

Shaking table tests are widely used to evaluate the seismic performance of buildings and infrastructure under earthquake excitations. In such tests, specimens are typically subjected to gradually increasing-amplitude accelerations, from small to large, until they reach ultimate failure. Consequently, specimens in shaking table tests are often nonlinear, sometimes exhibiting extreme nonlinearity, which in turn makes the dynamics of the shaking table

system complex and strongly nonlinear. The accuracy of waveform reproduction in shaking table tests depends significantly on the control scheme [1]. Several control strategies have been proposed to improve seismic waveform reproduction, including three-parameter control [2, 3], displacement control [4], and acceleration control [5]. To reproduce wideband excitations for large structures with strong nonlinear characteristics, Pan et al. [6] proposed a frequency-divided three-parameter control method for a double-layer shaking table (DLST). Similarly, Tian et al. [7] introduced a frequency-divided offline iterative control (OIC) method to reproduce wide-frequency-range reference signals for DLST systems. However, both methods have only been validated on small-scale shaking tables. The OIC method is typically employed to achieve high-precision waveform reproduction of shaking table inputs. For instance, Tagawa and Kajiwara [8] employed an iterative input reference correction method for the E-defense control system. This process was performed offline and required iterative adjustment of six-degree-of-freedom inputs, resulting in inefficiency. Ji et al. [9] proposed an open-loop inverse compensation method using model matching and H∞ controller design to improve the accuracy of seismic acceleration responses in substructures; however, this method was also implemented offline. Maddaloni et al. [10] developed an additional "open-loop" feedforward compensation method based on an inverse transfer function to achieve acceptable acceleration time histories for specimens. Zhou et al. [11] proposed a multidirectional decoupling iterative control method to reproduce acceleration in nonstructural shaking table tests. Both Maddaloni's and Zhou's methods are primarily suitable for nonstructural tests, and their applicability to general structural shaking table tests requires further investigation. As specimen nonlinearity develops and control–structure interaction increases, the accuracy of OIC diminishes. For shaking table tests of new structural systems—such as offshore wind turbine towers, underground space structures, and friction pendulum isolation structures [12]—OIC accuracy often requires improvement to achieve high precision [13, 14].

Although OIC can provide good tracking accuracy, it has several limitations. Achieving exact replication of the reference signal generally requires multiple iterations, which can cause cumulative damage to specimens. To address these shortcomings, several robust control methods have been applied to shaking tables. Chen et al. [15] proposed a model-based command-shaping controller in combination with conventional proportional–integral inner-loop control, offering a robust control framework. This method was validated using a flexible two-story steel specimen; however, its effectiveness for concrete structures remains to be studied. Adaptive control methods have also been applied to shaking tables to provide robust control over nonlinear ranges. For example, Neild et al. [16] proposed an adaptive substructure controller based on the minimum control synthesis approach, tested primarily on linear specimens. Enokida and Kajiwara [17] applied a nonlinear signal-based controller to nonlinear specimen tests, and both numerical and experimental results validated its efficiency and practicability. Other adaptive approaches include Yao et al. [18], who developed a least-mean-square (LMS) adaptive algorithm for harmonic elimination to reduce distortion and improve shaking table performance. A time-varying step-size LMS algorithm was introduced to enhance convergence; however, this method was tested only on sine waves and not on random or seismic signals. Dertimanis et al. [19] proposed an adaptive inverse control framework with an improved filtered-x LMS algorithm for accurate waveform reproduction; however, this required a lengthy learning process before inputting earthquake waveforms. Model-based controllers (MBCs) have also been investigated for improved acceleration tracking in nonlinear systems. Phillips et al. [20] and Phillips and Spencer [21] demonstrated the effectiveness of MBCs on unidirectional shaking tables with both linear and nonlinear structures. Najafi et al. [22] further developed a modified MBC strategy by introducing a stability condition to enhance robustness. To address modeling uncertainties and nonlinearities, Yang et al. [23] employed a sliding mode control technique to improve robustness; however, its acceleration tracking accuracy requires further refinement. More recently, hierarchical control strategies have been introduced. Yao et al. [24] and Chen et al. [25] developed an acceleration-based sliding-mode hierarchical control framework and a model reference adaptive hierarchical control framework. Rajabi et al. [26] applied extended Kalman filter/unscented Kalman filter (EKF/UKF) techniques for online state estimation of shaking table controllers. Ryu et al. [27] integrated a real-time EKF estimator with a feedback-linearization–based adaptive control method, demonstrating improved tracking and estimation performance. Although these methods have enhanced control accuracy, most of them have been validated only on small-scale shaking tables and steel specimens. Their control accuracy and stability still require verification and further study for large-scale shaking table tests on general concrete and reinforced concrete structures.

For large-scale shaking table model tests with degradation-type specimens, the real-time iterative control (RIC) method offers a potential solution ([28] MTS Website). Although it has been investigated by several researchers, further studies are required to improve its accuracy and stability for engineering applications. The concept of online iterative control was first proposed in the 1960s [29]. Mechanical Testing and Simulation (MTS) later developed software and applied the approach experimentally to certain specimens (MTS Website). However, online iterative control still requires significant improvements for general application beyond special cases, particularly with respect to stability. In shaking table tests involving specimens in the elastoplastic stage, a low acceleration iterative updating rate may lead to poor control accuracy. To address this issue, Tian et al. [30] proposed a fast-frequency segmental iterative control method. Nonetheless, the robustness of such methods has only been verified for small-scale steel-frame models with elastoplastic characteristics. Their accuracy tends to decrease once the specimens enter the elastoplastic stage, and the stability of these approaches remains a critical concern. For medium- and large-scale

shaking table model tests, ensuring the stability and reliability of RIC is essential. This requirement is largely determined by the performance of the online correction algorithm used for the RIC system matrix. To address these limitations, a RIC method with system matrix online correction (RICSC) is proposed. Zhang et al. [31] proposed the RICSC method for a shaking table test. To analyze the performance of the RICSC method, the effect of system matrix accuracy indices is analyzed in this study—the coherence function (CF) weighted sum, CF, and autocorrelation power density spectrum (AS)—and corrects the matrix using either frame correction (FC) or frequency point (FP) correction algorithms, and the effect of the initial system matrix known or unknown is also discussed. This ensures reliable tracking and high-precision waveform reproduction, thereby broadening the applicability of RIC to a wider range of structural shaking table tests.

The remainder of this paper is organized as follows. Section 2 presents the principles of the RICSC method. Section 3 verifies the RICSC approach through numerical simulation of a nonlinear specimen. Section 4 introduces the experimental system design for the RICSC method, and Section 5 analyzes the experimental verification results. Finally, Section 6 summarizes the conclusions drawn from the simulations and tests.

2. RIC Based on New System Matrix Online Correction Algorithm

The principle underlying the new method is that the effectiveness and accuracy of the identification of the system matrix are determined by the CF, weighted sum of CFs, or the power spectral density as a matrix accuracy evaluation index; if the matrix accuracy evaluation index meets the demand, the system matrix is corrected, and vice versa. The novelty of the RICSC method is that the online correction of the system matrix is based on new FC and FP correction algorithms, which exhibit enhanced accuracy and stability than the direct correction of traditional RIC. The generation of the initial command signal, loading and measurement of the response signal, identification of the system matrix, and iterative updating of the command signal processes were nearly identical as those in traditional IRC. Only the online correction of the system matrix of the RICSC is different from that of the traditional IRC. Online correction of the system matrix is a key part of the RICSC, which improves the accuracy and stability of the online correction process using FC and a FP correction algorithm. In this section, the basic diagram of the RICSC method is introduced, and the five processes of the RICSC method are analyzed.

2.1. Basic Diagram of the RICSC Method. The RICSC method corrects the system matrix online to improve waveform reproduction accuracy when the system characteristics change comparing with the initial state. As shown in Figure 1, the RICSC method consists of five processes: generation of the initial command signal, loading and measurement of the response signal, identification of the system matrix, online correction of the system matrix, and iterative updating of the command signal. The RICSC method decomposes the reference signal of the shaking table into segments, with each segment serving as the basic unit of the system matrix identified and corrected, called a frame. The length of the frame is determined according to several aspects: data points of a frame, calculation duration, signal frequency range, and sampling frequency of the measurement. The data points of a frame must be determined first because the different data point number can influence the calculation duration of the controller. The real-time identification and correction are conducted with frames as the basic unit. For example, when the data point number of a frame is set as $n = 1024$ in this study, the calculation duration of real-time iterative controller can be estimated. Subsequently, sampling frequency of the measurement f_s (the nomenclature is summarized in Appendix A) is set to make the sampling time step larger than the calculation duration. The frequency resolution [32] and frequency range of the fast Fourier transform (FFT) can be obtained as f_s/n and $f_s/n \sim f_s/2$, respectively. The signal frequency range can be determined when the specimen and the input signal to the shaking table are known. It must be satisfied that the frequency range of FFT is larger than approximately 4-5 times of the maximum frequency of the signal frequency range. If this condition cannot be satisfied, the length of the frame (data point number) should be adjusted again. The frequency resolution and the frequency range of the FFT will affect the control effect because the FFT is the basic calculation of the real-time iterative controller. The relation between the control effect and the length is dependent on the specimens and nonlinear characteristics. The signal frequency range of shaking table tests with different specimens with different nonlinear characteristics may have little bit difference. The length of the frame needs to be changed if the signal frequency range for the shaking table has obvious changes.

A frame is the basic unit for the five processes of the RICSC method. For example, when ground motion record at the El Centro Station in the 1940 Imperial Valley Earthquake is taken as the input, the acceleration of earthquake time history is divided into multiple frames (which have 10 frames). The first frame of the command signal was generated during the generation of the initial command signal. Subsequently, the command signal data points of this frame were input to load individually, and the response signals were measured synchronously, as shown in Figure 2. When the first frame of the command signal is loaded and measured, the system matrix and the matrix accuracy evaluation index of the frame signals can be identified. The system matrix is corrected based on the selected online correction algorithm. Then, the second frame of the command signal is iteratively corrected and input to the load individually. The next frame data of the command signals are corrected and loaded; therefore, it continues in a cycle until the last frame of the command signals is corrected and loaded (which is the 10th frame in this case). The time length of one frame is T, and the total time length of the reference signal in the shaking table test is defined as T_{total}. When the sampling

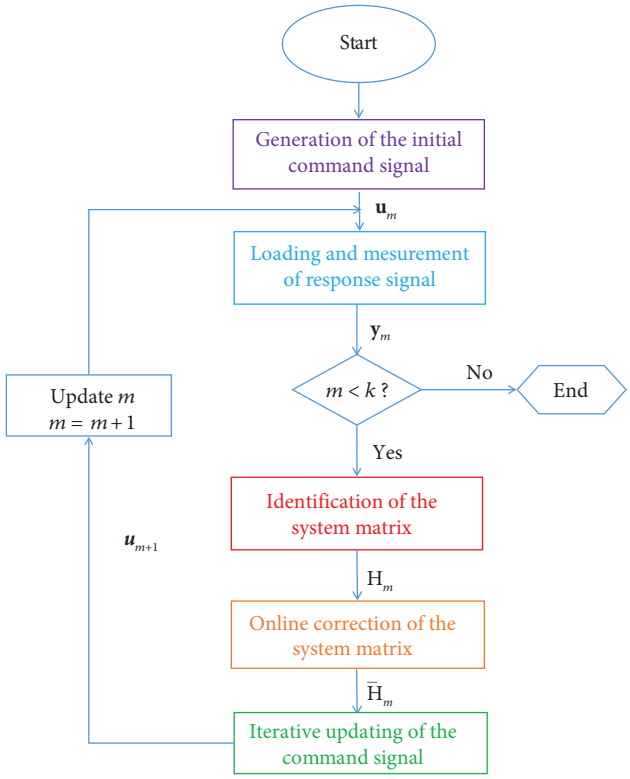

Figure 1: Schematic of the RICSC method.

frequency is defined as f_s, the number of data points in one frame is $n = T \times f_s$, and the number of frames of the reference signal is $k = T_{\text{total}}/T$. When the total time length of the test cannot be exactly divisible into T, zero-padding data are added at the end of the time history of the reference signal. This provides an option to satisfy the condition of being exactly divisible into T. The shaking table test was completed when the k^{th} frame command signals were loaded, and the k^{th} frame response signals were measured ($k = m$), as shown in Figure 1. The five processes of the RICSC method are described as follows.

2.2. Generation of the First Frame Command Signal. System matrix $\mathbf{H}$ is the key component for generating the command signal and is defined as the transfer function matrix of the shaking table system. The general expressions are given in the following equation.

$$\mathbf{H} = \begin{bmatrix} \frac{Y_1(s)}{X_1(s)} & \frac{Y_1(s)}{X_2(s)} & \cdots & \frac{Y_1(s)}{X_l(s)} \\ \frac{Y_2(s)}{X_1(s)} & \frac{Y_2(s)}{X_2(s)} & \cdots & \frac{Y_2(s)}{X_l(s)} \\ \vdots & \vdots & \ddots & \vdots \\ \frac{Y_l(s)}{X_1(s)} & \frac{Y_l(s)}{X_2(s)} & \cdots & \frac{Y_l(s)}{X_l(s)} \end{bmatrix}, \tag{1}$$

where $Y_i(s), i = 1, \ldots, l$ denotes the Laplace transform of the response signal of the shaking table system, $X_i(s), i = 1, \ldots, l$ denotes the Laplace transform of the command signal of the shaking table system, and l denotes the number of input and output signals.

The RICSC method first determines whether the initial system matrix $\mathbf{H}_0$ of the shaking table is known. The initial system matrix $\mathbf{H}_0$ can be obtained by an identification test with a band-limit white noise input. If the $\mathbf{H}_0$ is known, it can be used to generate the first-frame command signal. The $\tilde{\boldsymbol{y}}_1$ represents the time domain of the first-frame reference signal, which is transformed into the frequency-domain reference signal $\tilde{\boldsymbol{Y}}_1$ using a FFT. $\mathbf{G}_0$ denotes the inverse matrix of the initial system matrix $\mathbf{H}_0$, as shown in equation (2). When $\mathbf{H}_0$ is known, the frequency domain of the first-frame driving signal $\boldsymbol{U}_1$ can be obtained using equation (3). Subsequently, $\boldsymbol{U}_1$ is transformed into the first-frame driving signal $\boldsymbol{u}_1$ using an inverse fast Fourier transform (IFFT). If $\mathbf{H}_0$ is unknown, $\boldsymbol{u}_1$ is a white noise signal $\boldsymbol{u}_{\text{white noise}}$ without calculation. A block diagram for generating the initial command signal $\boldsymbol{u}_1$ is shown in Figure 3.

$$\mathbf{G}_0 = \mathbf{H}_0^{-1}, \tag{2}$$

$$\boldsymbol{U}_1 = \mathbf{G}_0 \times \tilde{\mathbf{Y}}_1. \tag{3}$$

2.3. Loading and Measurement of the Response Signal. A block diagram of the loading and measurement of the response signal is shown in Figure 2. The m^{th} frame command signal $\mathbf{u}_m$ contains n data points of the command signal $\{u_{m,i}\}_{i=1,2,\ldots,n}$ and is sequentially input into the shaking table system to load. The RICSC method checks whether $i < n$, if $i < n$, the loading and measurement continue until the m^{th} frame command signal is completely loaded ($i = n$). The m^{th} frame response signal $\mathbf{y}_m$ consists of n data points for the measured response signal.

2.4. System Matrix Online Identification. The system matrix is identified based on the m^{th} frame command and response signals. The command signal $\mathbf{u}_m$ and response signal $\mathbf{y}_m$ undergo FFT to obtain their frequency-domain responses $\mathbf{U}_m$ and $\mathbf{Y}_m$, respectively. The m^{th} frame–identified system matrix $\mathbf{H}_m$ is obtained using the AS $\mathbf{S}_{u_m u_m}$ and the cross-correlation power density (CPD) spectrum $\mathbf{S}_{u_m y_m}$. A block diagram for the identification of system matrix $\mathbf{H}_m$ is shown in Figure 4.

The $\mathbf{S}_{u_m u_m}$ of $\mathbf{u}_m$ and the $\mathbf{S}_{u_m y_m}$ between $\mathbf{u}_m$ and $\mathbf{y}_m$ are obtained using the average periodogram method (also called the Welch algorithm), and the calculation equations are as follows:

$$\boldsymbol{S}_{u_m u_m} = \frac{1}{MN}\sum_{j=1}^{M} U_{m_j} U_{m_j}^* \tag{4}$$

$$\boldsymbol{S}_{u_m y_m} = \frac{1}{MN}\sum_{j=1}^{M} U_{m_j} Y_{m_j}^* \tag{5}$$

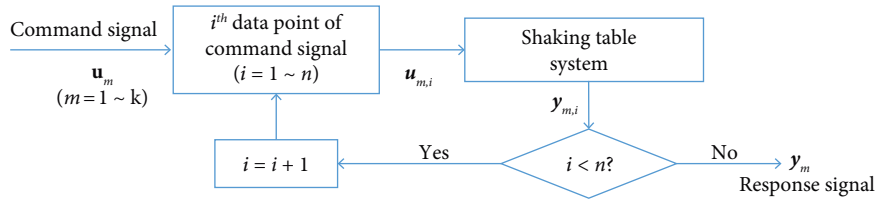

FIGURE 2: Block diagram of loading and measurement of the response signal.

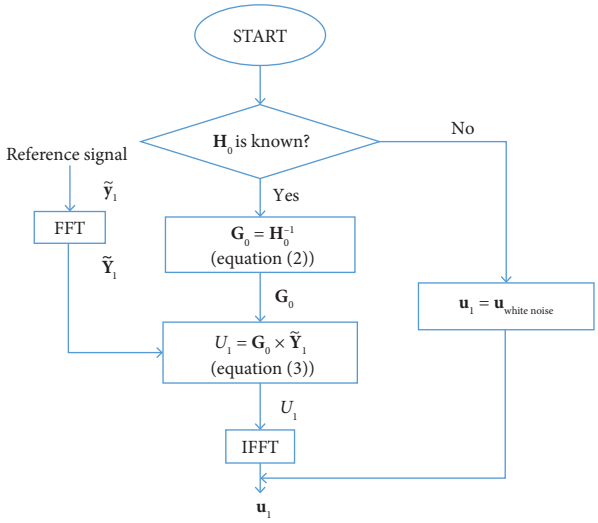

FIGURE 3: Block diagram of generation of the initial command signal.

where U_{m_j} and Y_{m_j} are the FFT of the j^{th} data segment of $\mathbf{u}_m$ and $\mathbf{y}_m$; $U^*_{m_j}$ and $Y^*_{m_j}$ are the complex conjugates of U_{m_j} and Y_{m_j}, respectively; M is the number of points in the average time; and N is the number of points in the FFT.

The identified system matrix $\mathbf{H}_m$ is calculated by the following equation:

$$\mathbf{H}_m = \mathbf{S}_{u_m y_m} \mathbf{S}^{-1}_{u_m u_m}. \tag{6}$$

The stability of the system matrix identified by the proposed approach can be ensured by checking whether the CF C_m is not within the [0~1] range. If the CF C_m of one frame is within the range [0-1], the system matrix calculated by using equation (7) can be considered as a stability system matrix. Otherwise, the system matrix cannot be identified by using equation (7), and the system matrix is forcibly set as a multiple matrix whose elements are $5 + 0i$. The CF C_m can be calculated based on $\mathbf{S}_{u_m u_m}$ and $\mathbf{S}_{u_m y_m}$ as follows.

$$C_m = \frac{\left|\mathbf{S}_{u_m y_m}\right|^2}{\mathbf{S}_{u_m u_m} \mathbf{S}_{y_m y_m}}, \tag{7}$$

where $\mathbf{S}_{y_m y_m}$ is the APD of Y_m:

$$\mathbf{S}_{y_m y_m} = \frac{1}{MN} \sum_{j=1}^{M} Y_{m_j} Y^*_{m_j}. \tag{8}$$

2.5. System Matrix Online Correction. After obtaining the system identification matrix $\mathbf{H}_m$, the system matrix was corrected using the online correction algorithm. Figure 5 shows the online correction process for the m^{th} frame of the system matrix. If the traditional RIC algorithm is selected, $\mathbf{H}_m$ can be used directly as the m^{th} frame system matrix. Otherwise, $\mathbf{H}_m$ is corrected to the m^{th} FC of the system matrix $\overline{\mathbf{H}}_m$ according to the matrix correction algorithm. There are two types of matrix correction algorithms: One is the FC algorithm, in which all elements of the system matrix are corrected together based on the CF weighting sum indicator, which is the weighting sum of all frequency points' CFs of a frame. The second is a FP correction algorithm, which uses a CF or power spectral density as the matrix accuracy evaluation index. The FP correction algorithm corrects every element of the system matrix separately, and the CF or AS of each element is checked.

If the online matrix identification algorithm is selected, $\mathbf{H}_m$ can be used directly as the m^{th} frame system matrix. Otherwise, $\mathbf{H}_m$ is corrected to the m^{th} frame of the system matrix $\overline{\mathbf{H}}_m$ according to the matrix correction algorithm. There are two types of matrix correction algorithms. The first is the FC algorithm, which uses the weighted sum of CFs as the matrix accuracy evaluation index to measure the accuracy of m^{th} frame $\mathbf{H}_m$. The second is a FP correction algorithm, which uses the CF or the power spectral density as the matrix accuracy evaluation index. The two matrix correction algorithms are introduced as follows.

2.5.1. FC Algorithm. In the FC algorithm, the system matrix is corrected according to the data from one frame. The evaluation index for the FC algorithm is the spectral density of the reference signal–weighted sum Φ_m.

The weight is the power spectral density $\mathbf{S}_{\tilde{y}_m \tilde{y}_m}$ of the reference signal $\tilde{\mathbf{y}}_m$ in the m^{th} frame.

$$\mathbf{S}_{\tilde{y}_m \tilde{y}_m} = \frac{1}{MN} \sum_{j=1}^{M} \tilde{Y}_{m_j} \tilde{Y}^*_{m_j}, \tag{9}$$

where $\tilde{Y}_{m_j}$ is the FFT of the j^{th} data segment of $\tilde{y}_m$ and $\tilde{Y}^*_{m_j}$ is the complex conjugate of $\tilde{Y}_{m_j}$.

$\mathbf{S}_{\tilde{y}_m \tilde{y}_m}$ is weighted by the CF $\boldsymbol{C}_m$ to obtain the m^{th} frame spectral density of the reference signal–weighted sum indicator Φ_m:

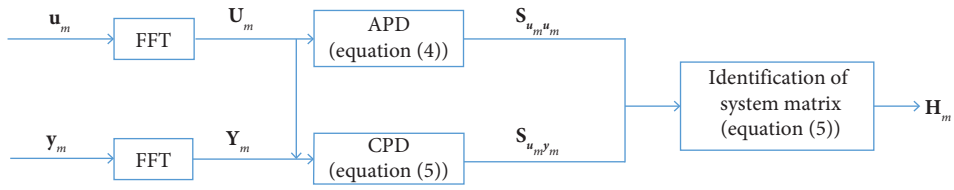

Figure 4: Block diagram of identification of the system matrix.

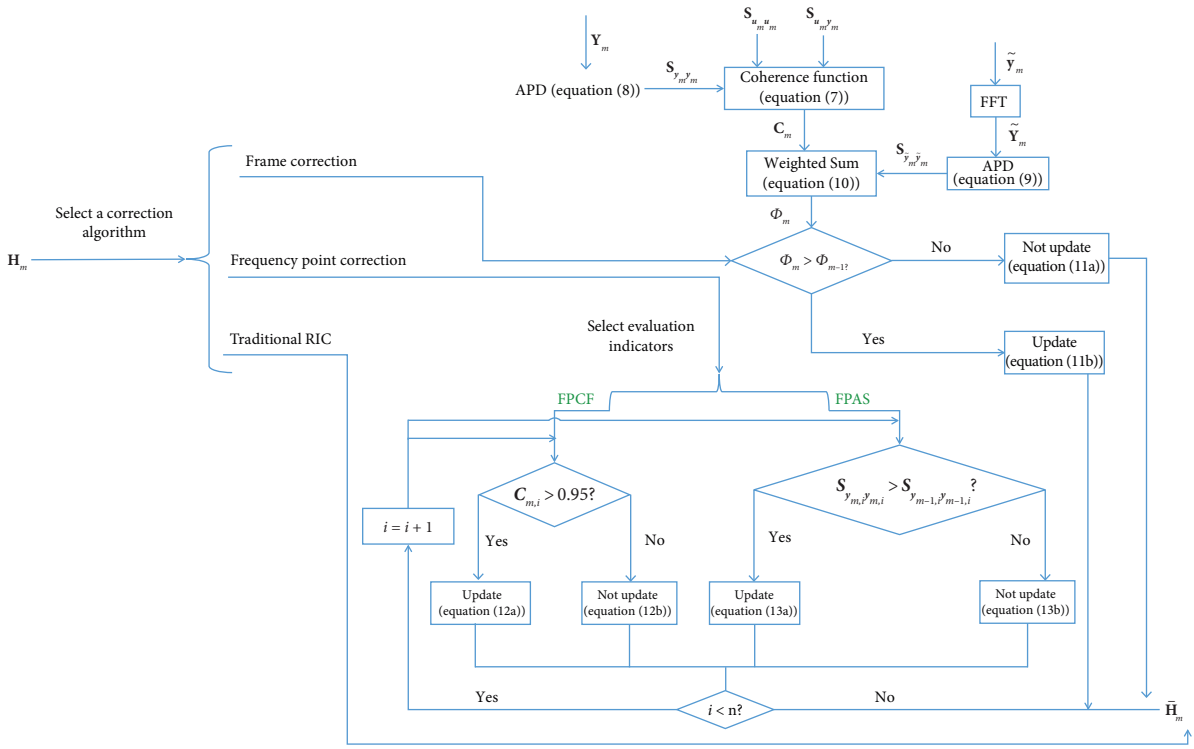

Figure 5: System matrix online correction block diagram.

$$\Phi_m = \sum_{i=1}^{n} S_{\tilde{y}_{m,i}\tilde{y}_{m,i}} C_{m,i}, \tag{10}$$

where $S_{\tilde{y}_{m,i}\tilde{y}_{m,i}}$ is the i^{th} frequency point of $S_{\tilde{y}_m\tilde{y}_m}$, and n is the number of data points involved in the weightin,g and $C_{m,i}$ is the i^{th} frequency point of $\mathbf{C}_m$.

Then, Φ_m is compared with the previous frame Φ_{m-1} to check whether Φ_m is greater than Φ_{m-1}. In this case, $\mathbf{H}_m$ is directly corrected to the $\overline{\mathbf{H}}_m$, that is, $\overline{\mathbf{H}}_m = \mathbf{H}_m$. Otherwise, the system matrix is not corrected, and the $m-1^{\text{th}}$ frame $\overline{\mathbf{H}}_{m-1}$ remains the system matrix of the m^{th} frame $\overline{\mathbf{H}}_m$, i.e., $\overline{\mathbf{H}}_m = \overline{\mathbf{H}}_{m-1}$.

$$\overline{\mathbf{H}}_m(f) = \mathbf{H}_m \quad (\Phi_m > \Phi_{m-1}), \tag{11a}$$

$$\overline{\mathbf{H}}_m(f) = \overline{\mathbf{H}}_{m-1} \quad (\Phi_m \leqslant \Phi_{m-1}), \tag{11b}$$

when $m = 1$, the correction of the system matrix is not performed, and the identified system matrix $\mathbf{H}_1$ is directly used as the system matrix of the shaking table system, that is, $\overline{\mathbf{H}}_1 = \mathbf{H}_1$.

2.5.2. FP Correction Algorithm. In the FP correction algorithm, the system matrix is corrected according to the CF or AS evaluation indices. The FP correction algorithm uses the CF and ASs as the matrix accuracy evaluation indices, abbreviated as FPCF and FPAS, respectively. The FPCF and FPAS algorithms are introduced as follows.

The concept of the FPCF algorithm is shown in Figure 6. Here, $H_{m,i}$ is the i^{th} frequency point of the $\mathbf{H}_m$ and $\overline{H}_{m-1,i}$ is the i^{th} frequency point of the $\overline{\mathbf{H}}_{m-1}$. The green dots in Figure 6 represent the frequency points of the $\mathbf{H}_m$, and the red dots represent the frequency points of the $\overline{\mathbf{H}}_{m-1}$. The yellow dotted line represents the CF limit $C_{\text{limit}} = 0.95$. When the CF at the frequency points $C_{m,i}$ above the yellow dotted line indicates that the accuracy of $H_{m,i}$ is satisfied, the corrected system matrix $\overline{H}_{m,i}$ is set as $H_{m,i}$, and vice versa; the corrected system matrix $\overline{H}_{m,i}$ is set as $\overline{H}_{m-1,i}$.

$$\overline{\mathbf{H}}_{m,i} = H_{m,i} \quad (C_{m,i} > 0.95), \tag{12a}$$

$$\overline{\mathbf{H}}_{m,i} = \overline{\mathbf{H}}_{m-1,i} \quad (C_{m,i} \leq 0.95), \tag{12b}$$

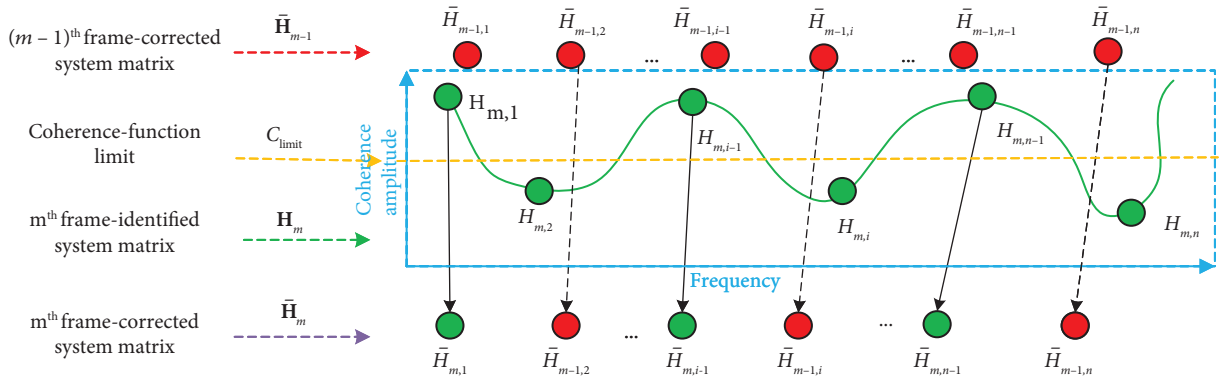

FIGURE 6: Schematic of the frequency point correction algorithm.

where $\overline{H}_{m,i}$ and $H_{m,i}$ denote the i^{th} frequency points of the $\overline{\mathbf{H}}_m$ and $\mathbf{H}_m$, respectively. $C_{m,i}$ denotes the CF of the i^{th} frequency point in the m^{th} frame.

The matrix accuracy evaluation index of the FPAS algorithm is the power spectral density. The FPAS algorithm corrects the system matrix based on whether the power spectral density $S_{y_{m,i}y_{m,i}}$ of the $\mathbf{H}_m$ is larger than the $S_{y_{m-1,i}y_{m-1,i}}$ of the $\mathbf{H}_{m-1}$. If the condition is satisfied, the i^{th} frequency point $H_{m,i}$ of the $\mathbf{H}_m$ is used as the i^{th} frequency point $\overline{H}_{m,i}$ of the $\overline{\mathbf{H}}_m$, i.e., $\overline{H}_{m,i} = H_{m,i}$. Otherwise, the i^{th} frequency point $\overline{H}_{m,i}$ of $\overline{\mathbf{H}}_m$ remains at the i^{th} frequency point $\overline{H}_{m-1,i}$ of the $\overline{\mathbf{H}}_{m-1}$, i.e., $\overline{H}_{m,i} = \overline{H}_{m-1,i}$.

$$\overleftarrow{\overline{\mathbf{H}}}_{m,i} = H_{m,i} \quad \left(S_{y_{m,i}y_{m,i}} > S_{y_{m-1,i}y_{m-1,i}}\right), \tag{13a}$$

$$\overleftarrow{\overline{\mathbf{H}}}_{m,i} = \overleftarrow{\overline{\mathbf{H}}}_{m-1,i} \quad \left(S_{y_{m,i}y_{m,i}} \le S_{y_{m-1,i}y_{m-1,i}}\right), \tag{13b}$$

where $S_{y_{m,i}y_{m,i}}$ denotes the APD of the m^{th} frame response signal at the i^{th} frequency.

When the n^{th} frequency point is corrected, the m^{th} frame-corrected system matrix $\overline{\mathbf{H}}_m$ is obtained.

2.6. Iterative Update of the Command Signal. The m^{th} frame-corrected system matrix is inverted to obtain the system's inverse matrix. To prevent instability caused by a singular matrix during the system matrix inversion process, two precautionary methods were implemented. First, the correction process was omitted if the AS of the response signal was excessively small. Second, by evaluating the magnitude of the system matrix, the correction process is omitted when the magnitude of the system matrix is too small, which prevents an infinite command signal when the system matrix is inversed. Because the FFT of the reference signal is known, the $m+1^{\text{th}}$ frame command signal can be calculated, updated, and defined as the new m^{th} frame command signal.

$$\mathbf{G}_m = \overline{\mathbf{H}}_{m-1}, \tag{14}$$

$$\boldsymbol{U}_{m+1} = \mathbf{G}_m \tilde{\boldsymbol{Y}}_m. \tag{15}$$

$\boldsymbol{U}_{m+1}$ is derived using the IFFT to obtain $\boldsymbol{u}_{m+1}$, and the frame number counter is increased to $m+1$. The new command signal was input to the shaking table for loading until the k^{th} frame command signal was loaded, which was at the end of the test. The iterative update of the command signal is shown in Figure 7.

3. Numerical Simulation of the Shaking Table Test With a Nonlinear Specimen

To study the effectiveness of the RICSC method, a numerical simulation of a shaking table test with a nonlinear specimen was conducted. The simulation model, reference signals, and results are presented below.

3.1. Numerical Simulation Model. The simulation model was developed using Simulink/MATLAB and compiled in SpeedGoat, a real-time simulation and testing system [33], as shown in Figure 8. The shaking table is employed displacement control as the inner-loop control, while the RICSC served as the outer-loop acceleration controller (Figure 8(a)). The RICSC generated command signals to control the motion of both the shaking table and the nonlinear specimen. The acceleration response signal of the shaking table was fed back to the RICSC to enable online iterations. The nonlinear simulation and dynamic actuator models are shown in Figures 8(b) and 8(d), respectively. In Figure 8(c), the actuator dynamics include the servovalve, actuator cylinder dynamic models, and the specimen.

The servovalve and actuator cylinder dynamic models were encapsulated as an S-function by BBK Test Systems Co., Ltd. [34]. The servovalve model incorporates a filter or delay to simulate phase shift and frequency response and applies an offset to account for overlap/deadband. As shown in Figure 8(d), the actuator-servovalve interaction was modeled with the actuator position and valve command signals as inputs and force as the output. The model accounted for pressure and force induced by flow, flow influenced by pressure and valve control signals, and added damping. Additionally, it incorporated forces due to differential pressure, pressure in each chamber, flow effects related to oil bulk modulus and volume changes, and flow variations with

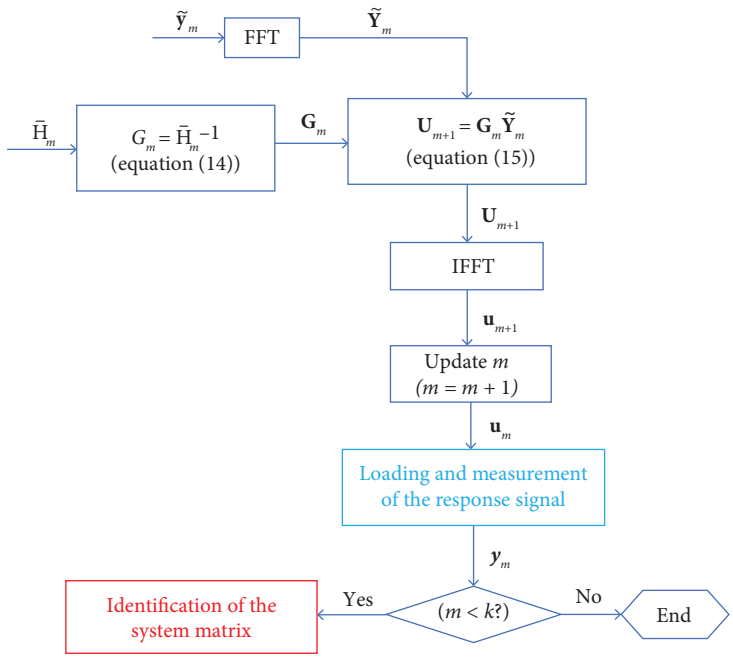

FIGURE 7: Iterative update of the command signal.

the actuator position. Cross-port bleeding, friction, damping, snubbers, and mechanical limitations were also considered [35]. Detailed formulations of the actuator model are omitted here for brevity. In Figure 8(b), the 'convert' block primarily converts input signals into specified data types or units. This block is compatible with various Simulink data types, including fixed-point numbers, floating-point numbers, integers, Boolean values, and enumerations.

The mass, damping, and initial stiffness of the SDOF specimens were 450 kg, 2500 N/ms^{-1}, and 17,765 N/m, respectively. The nonlinear spring model is illustrated in Figure 8(e). In this model, the output of the data-type conversion block is zero when $1 \geq |d|$ $(-1 \leq d \leq 1)$ and one when $|d| > 1$. The variable stiffness of the nonlinear spring is expressed as

$$K(d) = \begin{cases} K_0, & -1 \leq d \leq 1, \\ K_0 e^{(|d|-1)}, & 1 < |d|, \end{cases} \tag{16}$$

where $K_0 = 17765$ N/m is the initial stiffness of the spring and d is the displacement response. The nonlinear stiffness exhibits a hardening type, which poses a significant challenge in shaking table control.

3.2. Waveform Input. Two types of reference signals were used in the numerical simulations: an artificial wave and the El Centro 1940 Imperial Valley Earthquake ground motion record (Figure 9). The frequency range of the artificial wave was generally between 2 and 30 Hz, while that of the earthquake record was typically 2–25 Hz. The artificial wave energy was uniformly distributed across the frequency domain, covering a wide range of frequencies observed in recorded earthquake waveforms. The amplitude of the artificial wave acceleration was normalized to below 1 m/s^2. The amplitude of the y-directional acceleration of the El Centro ground motion record from the 1940 Imperial Valley Earthquake was scaled to 0.2 g because of the displacement limitation of the shaking table.

3.3. Simulation Results. Among the system matrix accuracy indices, the RICSC-FPCF method demonstrated the best control performance, as further discussed in Section 5. A comparison between the reference and response signals for the RICSC-FPCF algorithm under artificial wave excitation is shown in Figure 10.

As shown in Figure 10, the acceleration response signal closely matched the reference signal, demonstrating that the RICSC method can effectively control the shaking table under artificial wave excitation.

The results of the RICSC-FPCF and OIC methods under the El Centro Earthquake record are presented in Figure 11. It should be noted that the OIC method performed only one iteration. As illustrated in Figures 11(a) and 11(b), the response signal of the RICSC method was closer to the reference signal than that of the OIC method after a single iteration. To evaluate control accuracy, the mean absolute error (MAE) and root mean square error (RMSE) of the absolute error were calculated as follows:

$$\text{MAE} = \frac{1}{n \times m} \sum_{m=1}^{k} \sum_{i=1}^{n} \left| y_{m,i} - \tilde{y}_{m,i} \right|, \tag{17}$$

$$\text{RMSE} = \sqrt{\frac{1}{n \times m} \sum_{m=1}^{k} \sum_{i=1}^{n} \left(y_{m,i} - \tilde{y}_{m,i} \right)^2}. \tag{18}$$

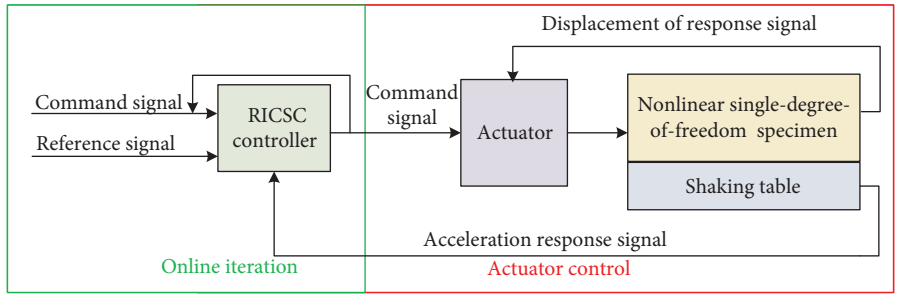

(a)

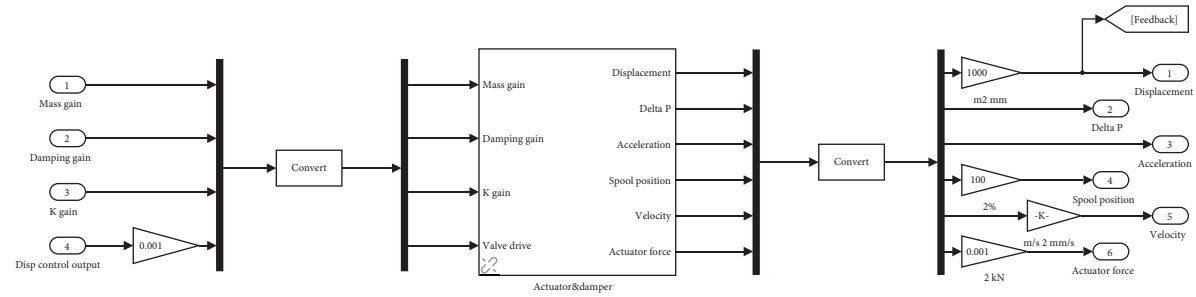

(b)

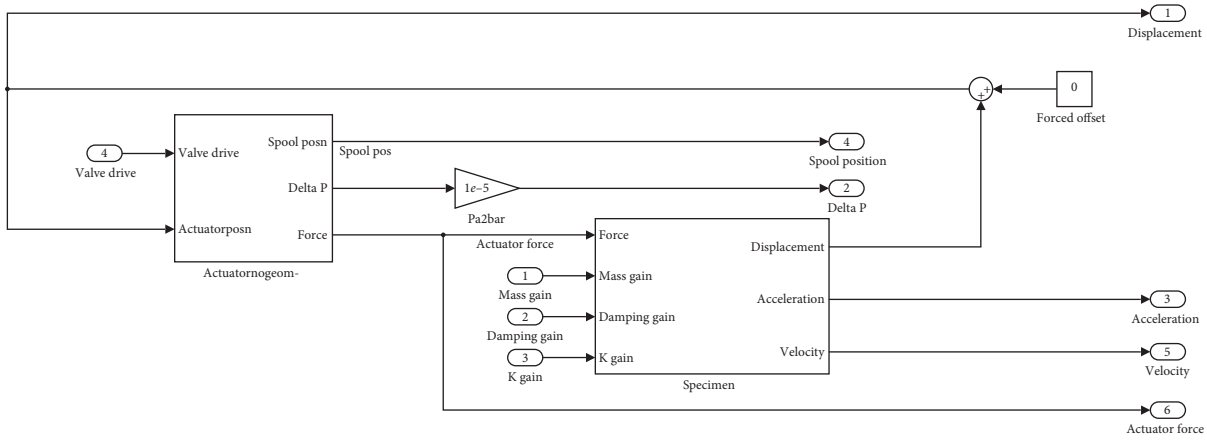

(c)

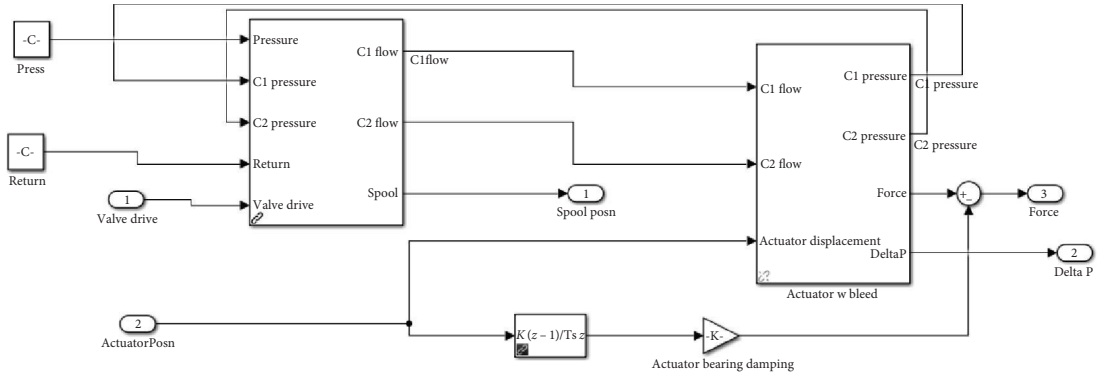

(d)

FIGURE 8: Continued.

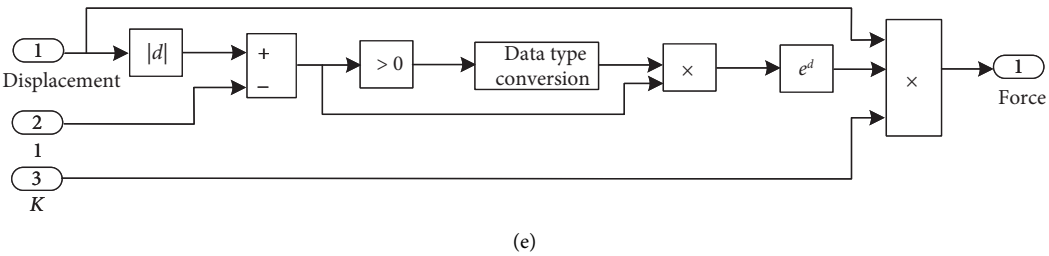

(e)

FIGURE 8: Nonlinear simulation model of the shaking table. (a) Flowchart of the RICSC simulation. (b) Nonlinear simulation. (c) Actuator model. (d) Servovalve and actuator cylinder dynamic model. (e) Nonlinear spring model.

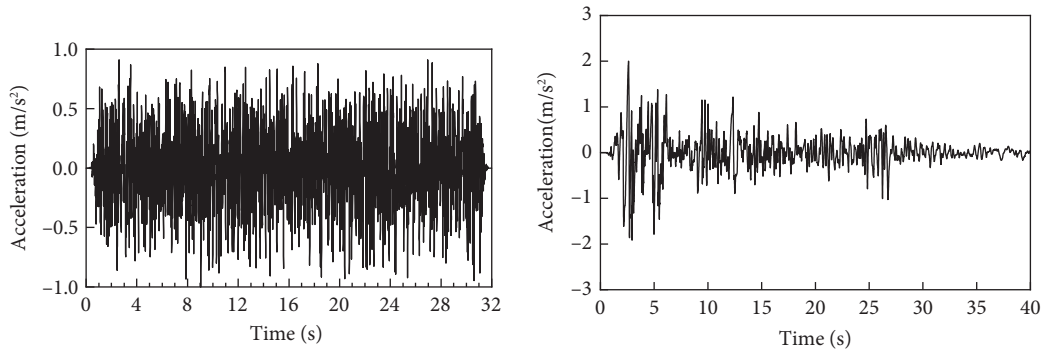

(a) (b)

FIGURE 9: Reference signal for the shaking table test simulation. (a) Artificial wave. (b) El Centro 1940 Imperial Valley Earthquake ground motion record.

From Figures 11(a) and 11(b), the response signal of the RICSC method was closer to the reference signal than that of the OIC method with the one-time test. For the RICSC method, the MAE was 0.1744 and the RMSE was 0.2390. For the OIC method, the MAE was 0.3239 and the RMSE was 0.5274. These results indicate that the reproduction accuracy of the RICSC method was superior to that of the OIC method in the one-time test. The RICSC method may be particularly suitable for shaking table tests involving specimens that are easily damaged, as it achieves high accuracy in fewer iterations. For more robust specimens, the OIC method with multiple iterations may achieve higher accuracy, though this comparison is not discussed in detail here. The nonlinearity of the specimen affects the characteristics of the shaking table system, potentially altering its system matrix. The RICSC method addresses this by identifying the current system matrix of the shaking table–specimen system and correcting it whenever changes are detected using matrix accuracy evaluation indices. As the specimen's displacement response increased, its stiffness also increased. As shown in the enlarged details in Figures 10(a) and 11(a), the acceleration response signals of the RICSC method tracked the reference signals well even at large amplitudes. This demonstrates the capability of the RICSC method to effectively manage system nonlinearities.

4. Experimental System Design

To further analyze the effectiveness of the RICSC method, experimental validation was carried out using a unidirectional shaking table at the Institute of Engineering Mechanics, China Earthquake Administration. The specimen used in the shaking table test was a tuned-mass damper (TMD) device [36], which employed friction damping and exhibited nonlinear characteristics (Figure 12). The mass, fundamental frequency, stiffness, and damping of the specimen were 500 kg, 1.948 Hz, 1896.93 N/m, and 220 Ns/m, respectively. The performance parameters of the shaking table are listed in Table 1. As shown in Table 1, the specimen mass reached the rated loading capacity of the shaking table. This increased both the friction damping and the difficulty of control because of the enhanced nonlinearity and uncertainties introduced into the test.

4.1. Shaking Table Test Platform. The RICSC framework for the shaking table test is illustrated in Figure 13. A Pulsar shaking table controller (Pulsar Controller [37], Website link) was employed as the inner-loop control unit, while the outer-loop RICSC controller was implemented through real-time communication using a shared memory card network (SCRAMNet [38], Website link). Acceleration response signals were measured and used for online identification and correction of the system matrix. The RICSC method was developed and compiled using Simulink/MATLAB (Version 8.3, R2014a) on a host PC. Prior to the experiment, the algorithm was compiled into an xPC target host computer, and data were transmitted via SCRAMNet.

Previous studies [31] have shown that using 1024 data points achieves an optimal balance between control accuracy and computational efficiency, as RIC requires extremely fast

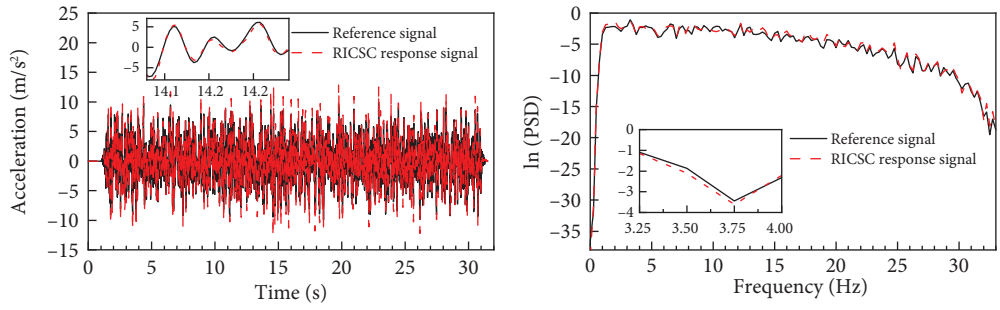

FIGURE 10: Comparison between reference and response signals under artificial wave excitation. (a) Time histories. (b) Power spectral densities.

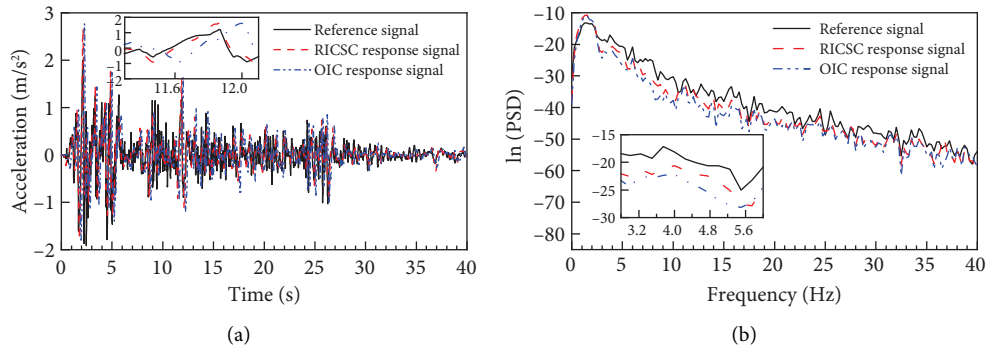

FIGURE 11: Simulation results of RICSC and OIC with one iteration. (a) Time histories. (b) Power spectral densities.

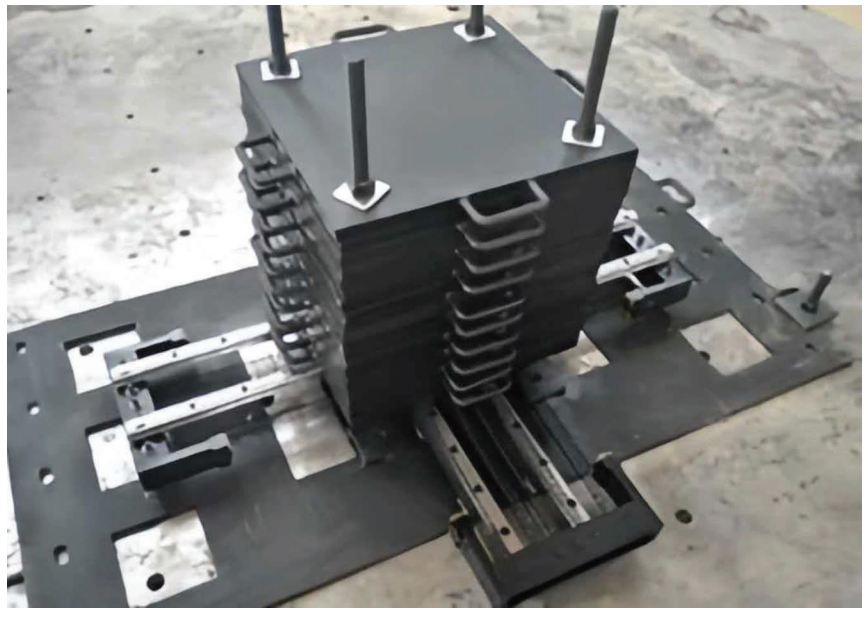

FIGURE 12: TMD specimen.

calculations. Because of space limitations, only the case of $T = 4$ s is discussed here. The sampling frequency was set at $f_s = 256$ Hz, the time length T was 4s, and the number n of data points per frame was 1024. The frequency range should be from 0.25 Hz to the half of the sampling frequency 128 Hz. This resulted in a frequency resolution of 0.25 Hz, which satisfies the accuracy requirement for reproducing earthquake waveforms.

Table 1: Shaking table performance parameters.

Parameters	Values
Rated frequency (Hz)	100
Rated load (kg)	500
Rated acceleration (g)	2.0
Rated speed (m/s)	0.9
Table size (m × m)	1.05 × 1.05

4.2. Test Conditions. To study the performance of the RICSC method, shaking table tests were conducted using reference signals, as described in Section 3. The RICSC requires substantial computational resources and relies on numerous FFTs and IFFTs. Therefore, extensive tests under different operating conditions were necessary to detect and eliminate logical errors and reduce the risk of potential data overflow. The control performance of the RICSC method with three correction algorithms (FC, FPCF, and FPAS) was compared with that of the traditional RIC method, which applies online matrix identification without correction. All four algorithms were tested using an unknown initial system matrix. In addition, the RICSC method with the FPCF algorithm was compared with OIC to demonstrate its superiority. For fairness, the initial matrices used in both methods were identified using the OIC approach. Table 2 summarizes the test conditions.

5. Shaking Table Test Results

Twenty test cases, listed in Table 2, were conducted. The results are discussed in two groups: those based on artificial wave input and those based on the El Centro 1940 Imperial Valley Earthquake ground motion records.

5.1. Artificial Wave Input. Shaking table tests were performed under an artificial wave input using traditional RIC, RICSC-FC, RICSC-FPCF, RICSC-FPAS, and OIC methods with both unknown and known initial system matrices.

5.1.1. Initial System Matrix Unknown. Figures 14 and 15 present the absolute error between the response and reference signals of the shaking table and a comparison of their power spectral densities, respectively.

As shown in Figure 14, the absolute errors of the traditional RIC, RICSC-FPCF, and RICSC-FPAS algorithms gradually decreased within 0–12 s, while the RICSC-FC algorithm showed no significant change. Because artificial waves have a wide frequency range, the RICSC-FC algorithm requires more data to accurately identify the system matrix when the initial matrix is unknown. Nevertheless, the error peaks of the RICSC-FC were smaller than those of the traditional RIC, RICSC-FPCF, and RICSC-FPAS algorithms. For comparison, the power spectral densities of the four algorithms in the frequency range of 5-6 Hz were enlarged (Figure 15). The results indicate that the control accuracies of the traditional RIC, RICSC-FPCF, and RICSC-FPAS algorithms were essentially the same and superior to those of the RICSC-FC.

5.1.2. Initial System Matrix Known. When the initial system matrix is known, the RICSC method can calculate the command signal based on it, thereby improving control accuracy. Figures 16 and 17 show the absolute errors between the response and reference signals and the corresponding power spectral densities for the four algorithms.

As shown in Figure 16, the control performance of all four algorithms was essentially the same, with absolute errors gradually decreasing after 12 s. Figure 17 demonstrates that the response signals closely matched the reference signals. Among the four, the RICSC with the FPCF algorithm achieved the best control performance.

5.1.3. Comparison With the OIC Method. To evaluate the control effectiveness of the RICSC, the OIC method was compared with the RICSC-FPCF algorithm using a known initial system matrix, which is shown in Section 5.1.2 to provide the best performance. The OIC method was conducted as a one-time test, and the system matrix it identified was used as the initial system matrix for the RICSC-FPCF to ensure fairness. Figures 18 and 19 present the absolute errors between the response and reference signals and power spectral densities of the RICSC-FPCF and OIC methods, respectively. As shown in Figure 18, the absolute errors of the RICSC-FPCF gradually converged after several iterations, whereas those of the OIC method showed minimal change. Both the MAE and RMSE of the RICSC were significantly smaller than those of the OIC method after one test.

As illustrated in Figure 19, the response signal of the RICSC-FPCF tracked the reference signal more closely than that of the OIC method. However, noticeable differences remained in the 5–15 Hz frequency range. This can be attributed to the relatively small amplitude of the selected initial system matrix at medium and high frequencies, which increased the amplitude of the inverse system matrix and slightly amplified the responses compared with the reference signals. Overall, when a one-time test was conducted, the RICSC-FPCF method with a known initial system matrix provided enhanced control accuracy than the OIC method.

5.2. El Centro 1940 Imperial Valley Earthquake Ground Motion Record Input. The shaking table test results under the 1940 Imperial Valley Earthquake ground motion record at the El Centro Station were evaluated using the traditional RIC, RICSC-FC, RICSC-FPCF, RICSC-FPAS, and OIC methods, with both unknown and known initial system matrices.

5.2.1. Initial System Matrix Unknown. Comparisons between the acceleration response and reference signals in the time domain and the corresponding power spectral densities obtained with the four algorithms are presented in Figures 20 and 21. As shown in the local magnifications of Figures 20 and 21, the RICSC-FPCF and RICSC-FPAS algorithms achieved marginally better control effects than the FC and traditional RIC algorithms. However, the overall control accuracies of all four algorithms were similar.

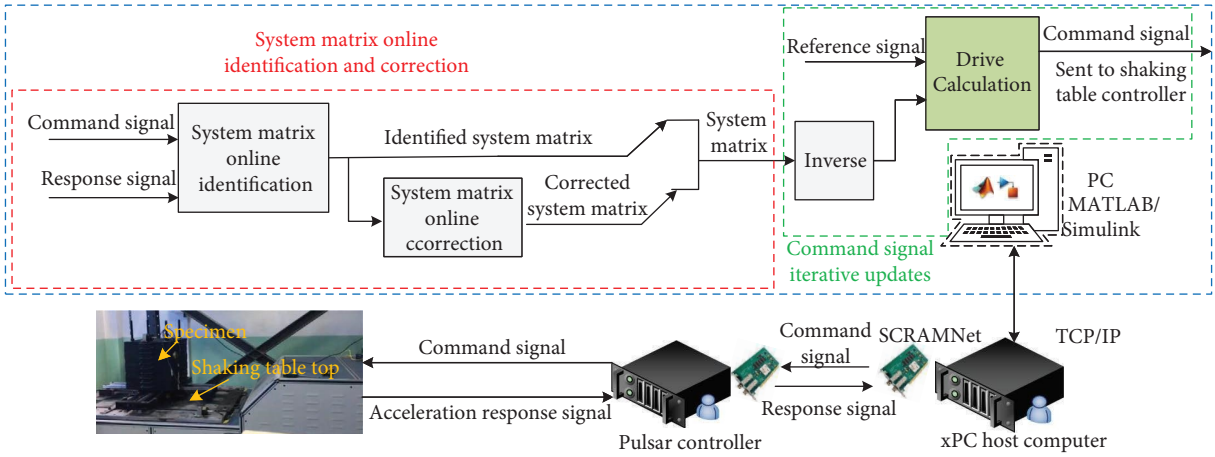

Figure 13: RICSC flowchart for the shaking table test.

Table 2: Test conditions.

Reference signal	Method	Initial system matrix	System matrix correction algorithm	Testing cases
Artificial wave	RICSC	Unknown	Traditional RIC	1
			FPCF	2
			FPAS	3
			FC	4
		Known	Traditional RIC	5
			FPCF	6
			FPAS	7
			FC	8
		OIC with one-time iteration		9
		RICSC-FPCF with the initial system matrix identified by OIC		10
Ground motion record at El Centro Station in the 1940 Imperial Valley Earthquake	RICSC	Unknown	Traditional RIC	11
			FPCF	12
			FPAS	13
			FC	14
		Known	Traditional RIC	15
			FPCF	16
			FPAS	17
			FC	18
		OIC with one-time iteration		19
		RICSC-FPCF with the initial system matrix identified by OIC		20

5.2.2. Initial System Matrix Known. Figures 22 and 23 show the comparison between the response and reference signals in the acceleration time domain and power spectral density, respectively. The middle and later portions of the El Centro ground motion record consist mainly of high-frequency, small-amplitude signals. Consequently, the acceleration amplitude of the shaking table was close to the noise generated by the actuator. As shown in Figure 23, the response signal deviated from the reference signal in the 12–20-Hz range. From the local magnifications of Figures 22 and 23, the RICSC-FPCF and RICSC-FPAS algorithms provided marginally better control performance than the RICSC-FC and traditional RIC methods.

5.2.3. Comparison Between RICSC and OIC Methods. To further evaluate control performance, the RICSC-FPCF algorithm was compared with the OIC method using a one-iteration test. The time histories, power spectral densities, and response absolute errors under the reference and response signals for the RICSC-FPCF and OIC methods are shown in Figures 24 and 25. As shown in Figure 24, the time differences between the reference and response signals were smaller for the RICSC-FPCF algorithm than for the OIC method. The RICSC method also exhibited enhanced control accuracy in the 3–10-Hz range. Figure 25 further indicates that both the MAE and RMSE of the RICSC method were smaller than those of the OIC method. Therefore, the RICSC-FPCF algorithm demonstrated higher control accuracy than the OIC method with one-time iterations under the El Centro 1940 Imperial Valley Earthquake ground motion input.

5.3. Error Evaluation. The MAE and RMSE values between the target and response signals for the 20 test cases are listed in Table 3.

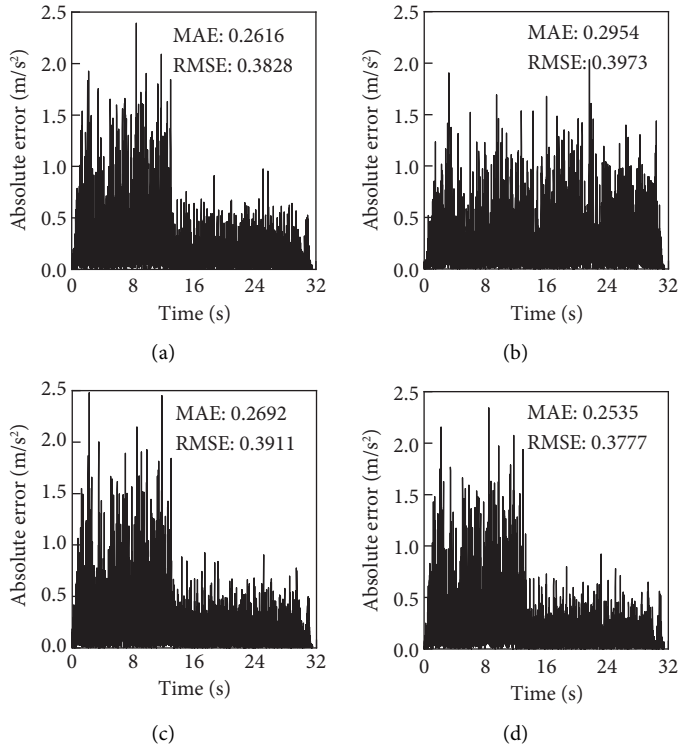

FIGURE 14: Absolute error of RICSC with unknown initial system matrix. (a) Traditional RIC. (b) Frame correction. (c) FPCF. (d) FPAS.

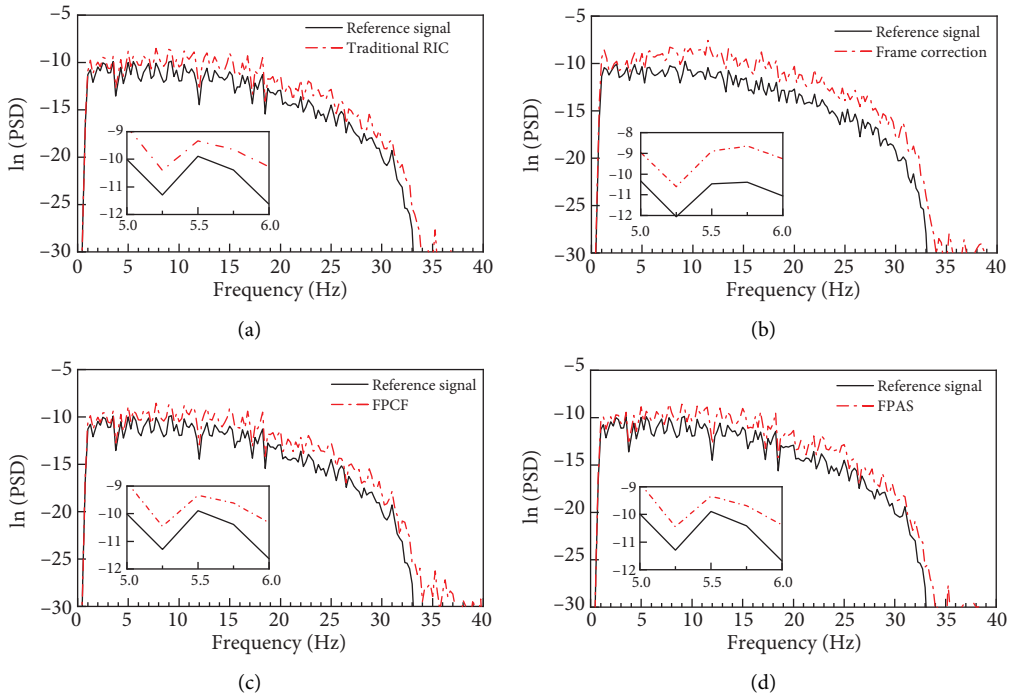

FIGURE 15: Power spectral density of RICSC with unknown initial system matrix. (a) Traditional RIC. (b) Frame correction. (c) FPCF. (d) FPAS.

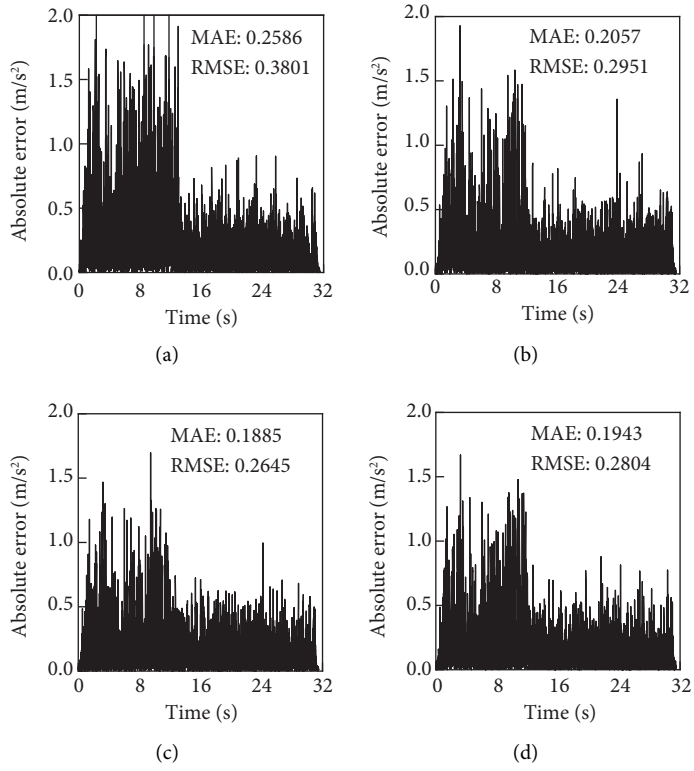

FIGURE 16: Absolute error of RICSC with known initial system matrix. (a) Traditional RIC. (b) Frame correction. (c) FPCF. (d) FPAS.

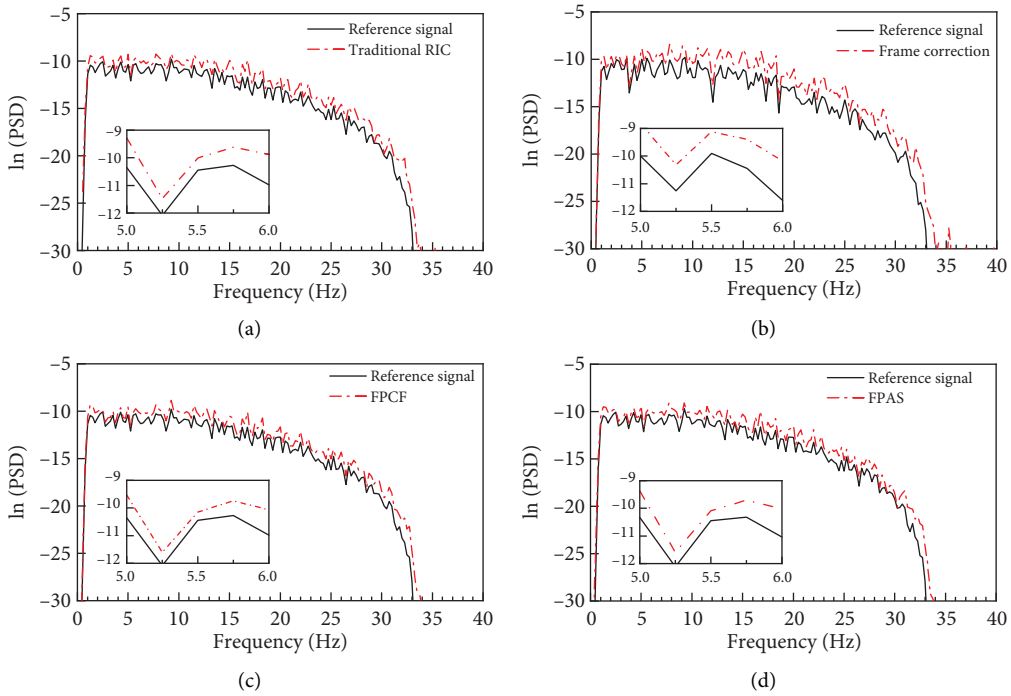

FIGURE 17: Power spectral density of RICSC with known initial system matrix. (a) Traditional RIC. (b) Frame correction. (c) FPCF. (d) FPAS.

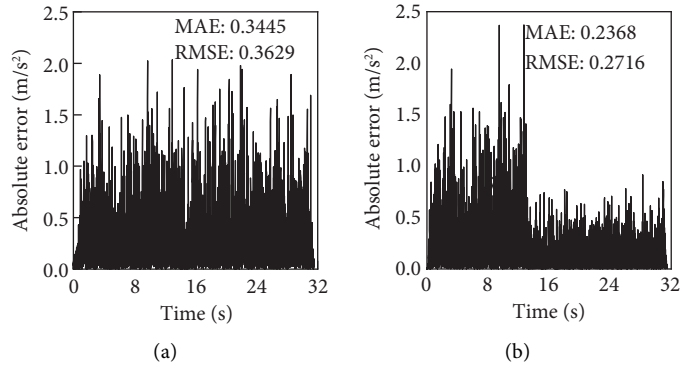

FIGURE 18: Absolute error of OIC and RICSC methods. (a) OIC. (b) RICSC.

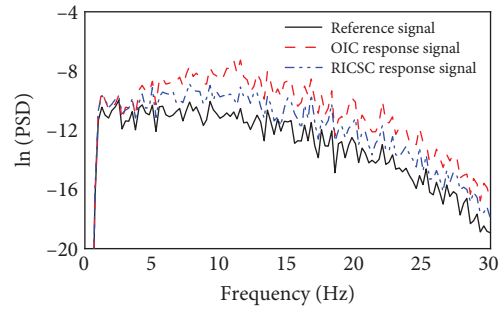

FIGURE 19: Power spectral density of RICSC-FPCF and OIC methods.

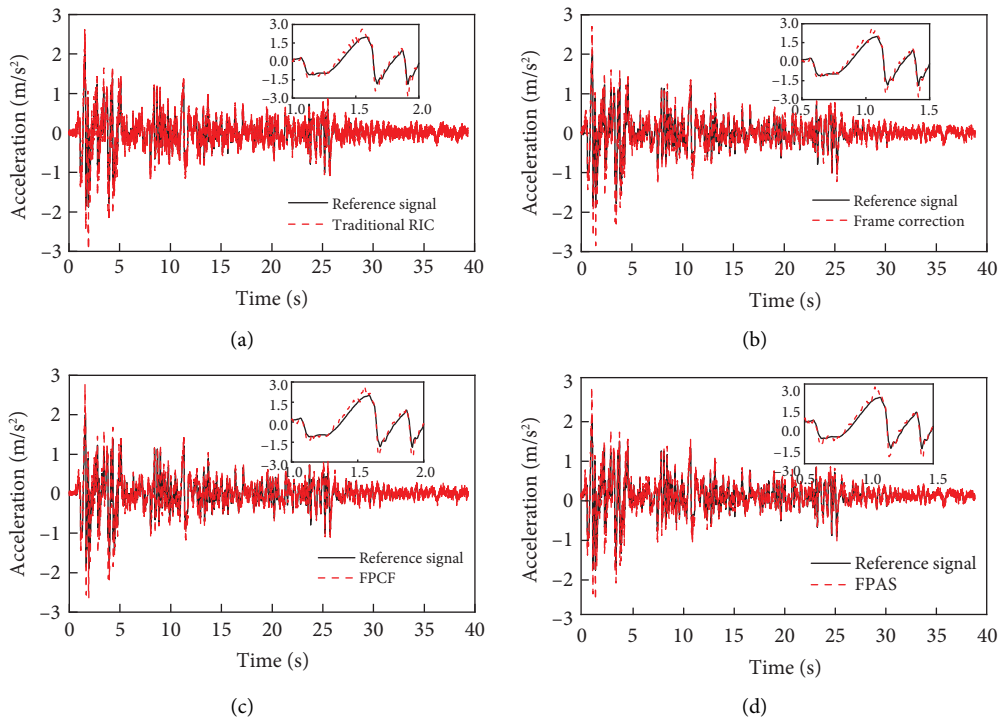

FIGURE 20: Comparison between reference and response signals with unknown initial system matrix. (a) Traditional RIC. (b) Frame correction. (c) FPCF. (d) FPAS.

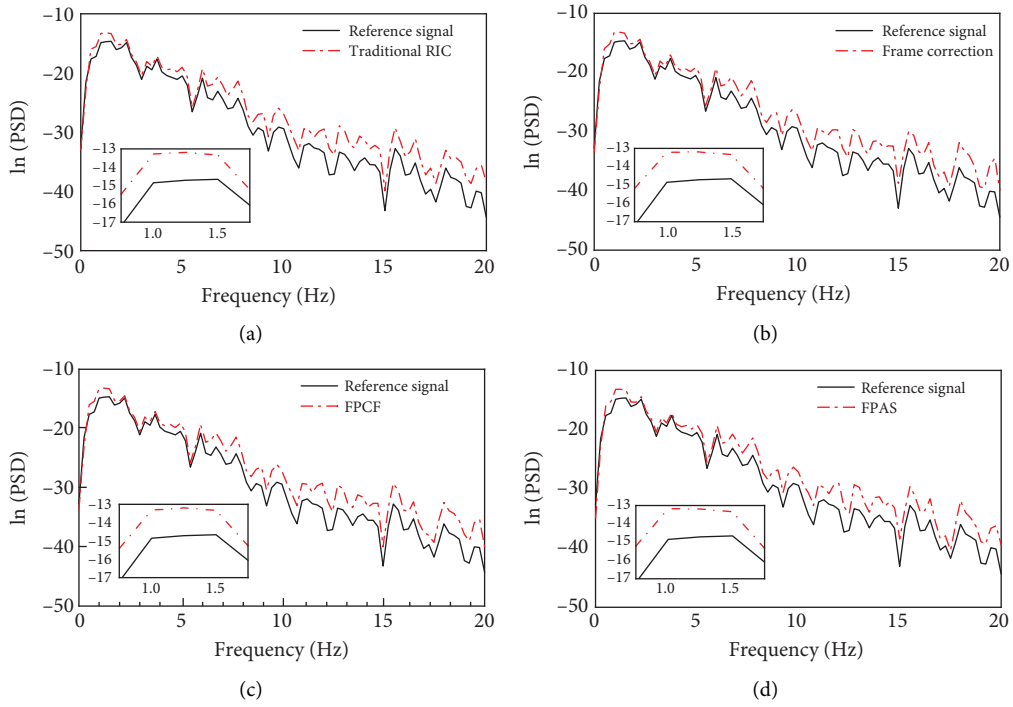

FIGURE 21: Power spectral density of RICSC with unknown initial system matrix. (a) Traditional RIC. (b) Frame correction. (c) FPCF. (d) FPAS.

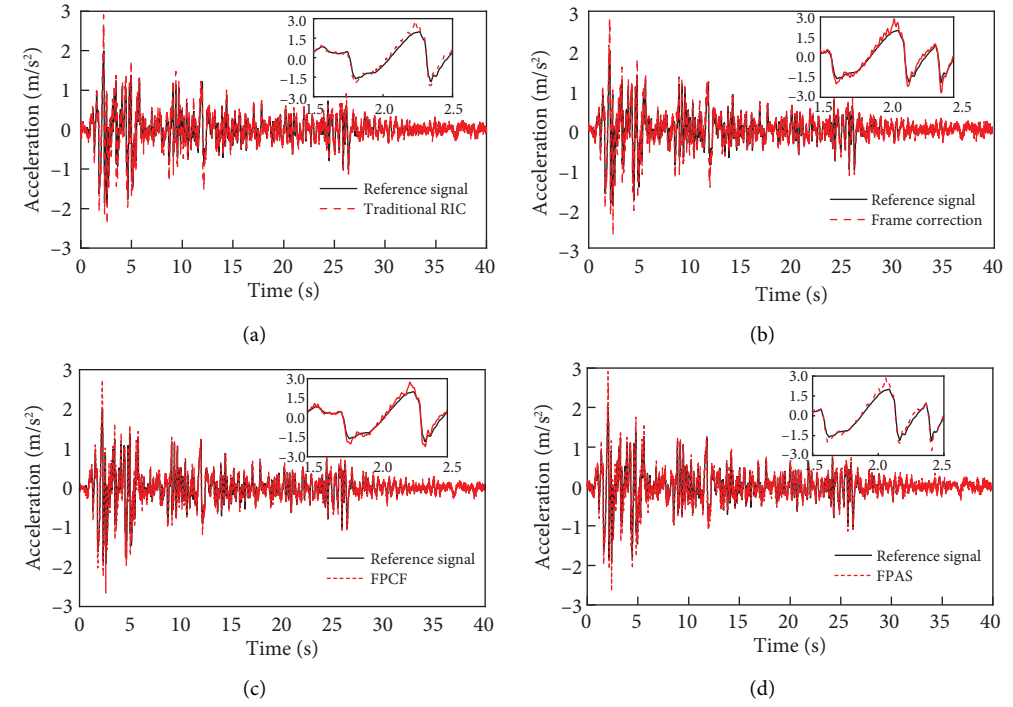

FIGURE 22: Comparison between reference and response signals with known initial system matrix. (a) Traditional RIC. (b) Frame correction. (c) FPCF. (d) FPAS.

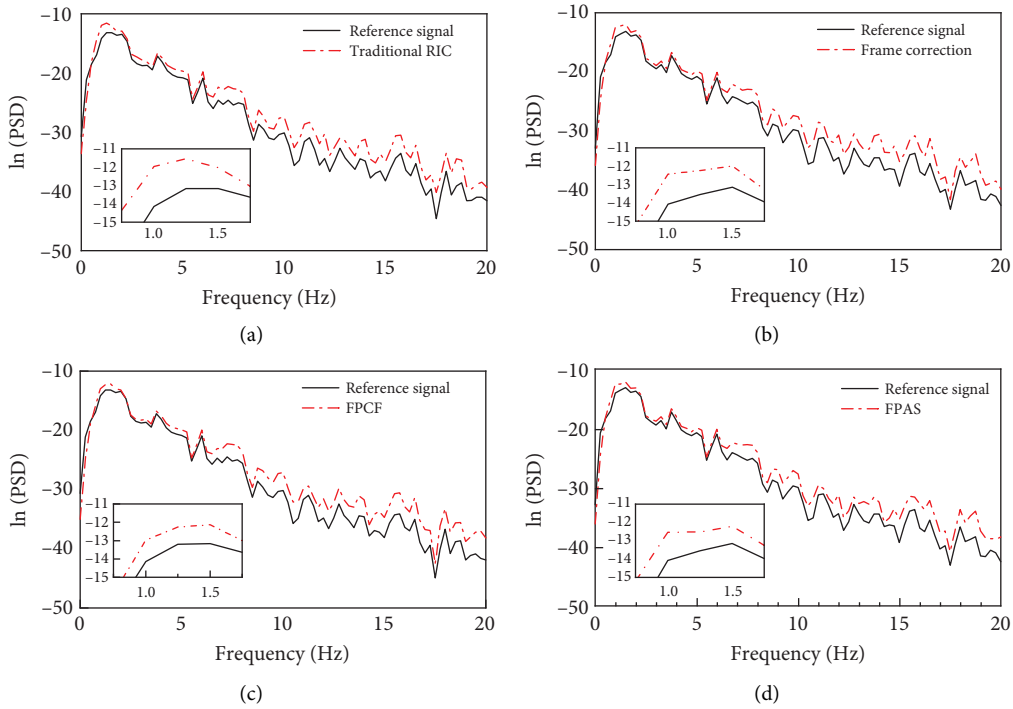

FIGURE 23: Power spectral density of RICSC with known initial system matrix. (a) Traditional RIC. (b) Frame correction. (c) FPCF. (d) FPAS.

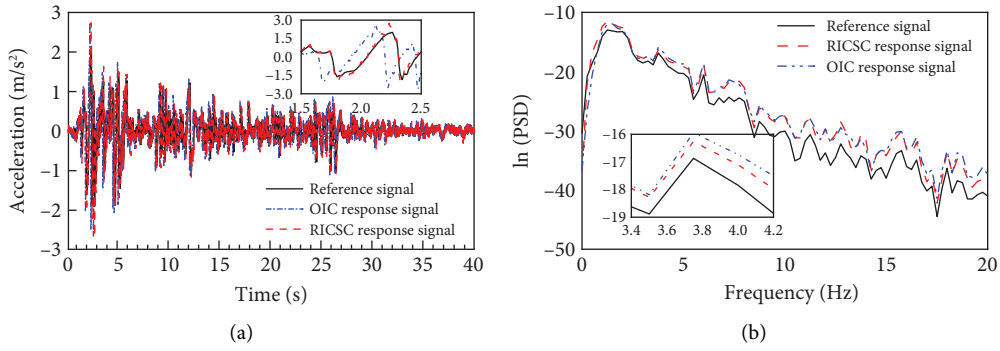

FIGURE 24: Comparison between accelerations obtained with OIC and RICSC. (a) Time histories. (b) Power spectral densities.

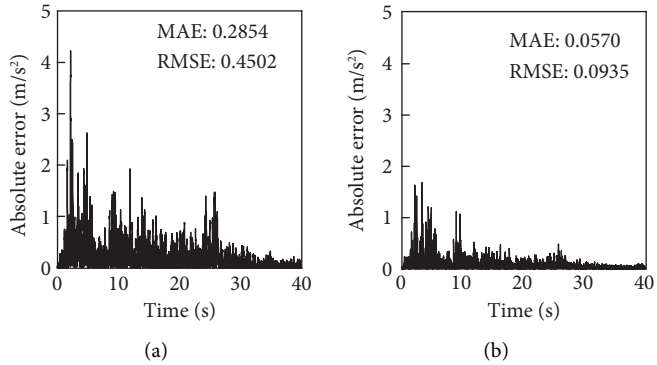

FIGURE 25: Response absolute error. (a) OIC. (b) RICSC.

Table 3: Mean absolute root mean square errors.

Test cases	Waveform input	Initial system matrix	Algorithm	MAE (m/s^2)	RMSE (m/s^2)
1	Artificial waveform	Unknown	Traditional RIC	0.2616	0.3828
2			FPCF	0.2692	0.3911
3			FPAS	0.2535	0.3777
4			FC	0.2954	0.3973
5		Known	Traditional RIC	0.2586	0.3801
6			FPCF	0.1885	0.2645
7			FPAS	0.1943	0.2804
8			FC	0.2057	0.2951
9		OIC with one-time iteration		0.3445	0.3629
10		RICSC-FPCF with the initial system matrix identified by OIC		0.2368	0.2716
11	Ground motion record at El Centro Station in the 1940 Imperial Valley Earthquake	Unknown	Traditional RIC	0.0795	0.1133
12			FPCF	0.0761	0.1100
13			FPAS	0.0720	0.1067
14			FC	0.0783	0.1120
15		Known	Traditional RIC	0.0813	0.1181
16			FPCF	0.0614	0.0902
17			FPAS	0.0689	0.0971
18			FC	0.0767	0.1123
19		OIC with one-time iteration		0.2854	0.4502
20		RICSC-FPCF with the initial system matrix identified by OIC		0.0570	0.0953

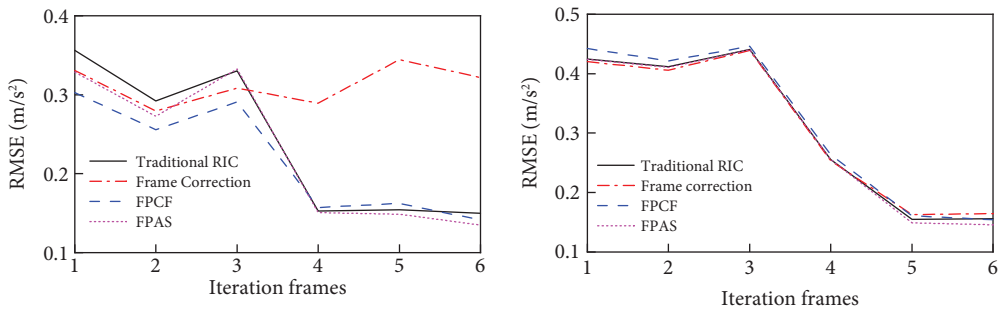

Figure 26: RMSE in Frames 1 to 6 under artificial wave. (a) Initial system matrix unknown. (b) Initial system matrix known.

The results of test Cases 1–8 indicate that the MAE and RMSE values of the four algorithms with a known initial system matrix were lower than those without it. In addition, the RICSC-FPCF and RICSC-FPAS methods outperformed the conventional RIC method. For test Cases 9 and 10, the RICSC-FPCF achieved smaller MAE and RMSE values than the OIC method.

Under the El Centro ground motion input (Cases 11–18), the RICSC-FPCF, RICSC-FPAS, and RICSC-FC methods with a known initial system matrix performed better than those without it. By contrast, the traditional RIC method without an initial system matrix marginally outperformed its counterpart with a known matrix, as seen in Cases 11 and 14. This is because the El Centro ground motion record is concentrated at low frequencies, where the RIC method with a known initial matrix used less data and identified the system matrix less effectively than when the initial matrix was unknown. For Cases 15–18, when the initial system matrix was known, the MAE and RMSE of the RICSC-FPCF and RICSC-FPAS methods were smaller than those of the RICSC-FC and traditional RIC methods. In test Cases 19 and 20, the RICSC-FPCF method again achieved smaller MAE and RMSE values than the OIC method.

Overall, across all 20 cases, the results confirm that the RICSC-FPCF method provided enhanced control accuracy than both the traditional RIC and OIC methods.

To compare the RMSE throughout the process, the RMSE between the response and reference signals for Frames 1–6 of the traditional RIC, RICSC-FC, RICSC-FPCF, and RICSC-FPAS methods under two inputs are shown in Figures 26 and 27, respectively.

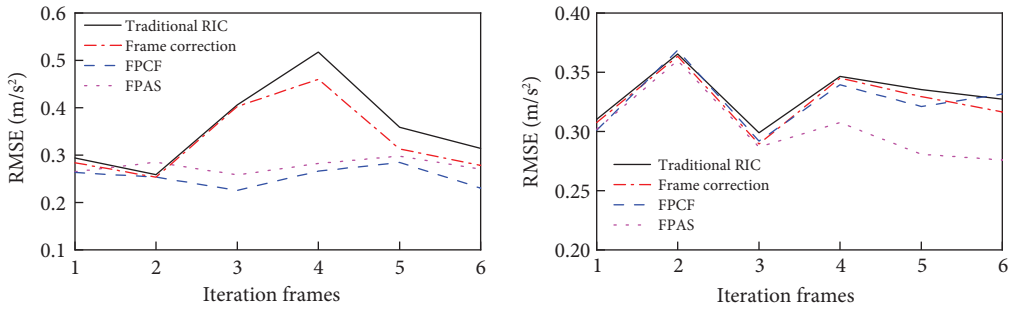

FIGURE 27: RMSE in Frames 1 to 6 under El Centro 1940 Imperial Valley Earthquake ground motion record. (a) Initial system matrix unknown. (b) Initial system matrix known.

From Figure 26, (i) the RICSC-FPCF and RICSC-FPAS methods converged fastest, irrespective of whether the initial system matrix was known, and (ii) the convergence of RICSC-FC was strongly affected by the initial system matrix: It did not converge when the initial matrix was unknown but did converge when the matrix was known. From Figure 27, (i) the RICSC-FPCF method converged fastest when the initial system matrix was unknown and (ii) when the matrix was known, the convergence rates of all four methods were similar, with RICSC-FPAS showing the best convergence. As illustrated in Figures 26 and 27, the RICSC-FPCF and RICSC-FPAS methods consistently achieved higher control accuracy than the traditional RIC and RICSC-FC methods, regardless of whether the initial system matrix was known.

6. Summary

In this study, a RIC method based on a system matrix online correction algorithm was studied to improve the reproduction accuracy of shaking table tests. The RICSC method employs three matrix accuracy evaluation indices to assess system matrix identification accuracy and applies online correction algorithms based on these indices, and use the initial system matrix identified in advance to improve the control performance. The RICSC method was implemented using both software and a hardware platform based on a shaking table. A shaking table test was performed with a TMD specimen. The control performance of the RICSC in a nonlinear system was verified through numerical simulations using either an artificial waveform or the ground motion record from the El Centro Station during the 1940 Imperial Valley Earthquake as reference signals. The RICSC method, incorporating three matrix correction algorithms, was compared with the traditional RIC, and the RICSC method with the FPCF algorithm was further compared with the OIC method to verify its superiority. The key conclusions are as follows:

1. Whether the initial system matrix is unknown or known, the RICSC method using the FP correction algorithm achieves higher control accuracy than both the FC algorithm and the traditional RIC algorithm.
2. When the initial matrix is known, the target waveform reproduction accuracy is higher than when it is unknown. In this case, the error between the response acceleration and target waveform obtained using the FPCF method is minimized.
2. When the initial matrices are known and identical, the RICSC method with the FPCF algorithm achieves significantly higher accuracy in reproducing the target waveform than the OIC method after the first iteration.
3. For systems with nonlinear characteristics, the RICSC method improves shaking table acceleration reproduction accuracy by adopting the FP correction algorithm with a CF as the matrix accuracy evaluation index. Its reproduction accuracy of the target waveform is higher than that of the OIC method.

Furthermore, the RICSC algorithm was validated using a unidirectional shaking table. Future work will apply the algorithm to a three-direction, six-degree-of-freedom shaking table to investigate its effectiveness for multi-degree-of-freedom shaking table tests.

Appendix A

The nomenclature was added on the simple names used in the context that groups the notations based on their dimensions (Tables A1, A2, and A3).

Table A1: Scalar.

$\mathbf{C}_{m,i}$	Coherence function of $\mathbf{C}_m$ at the i^{th} frequency point
d	Displacement response
f_s	Sampling frequency
$\mathbf{H}_{m,i}$	i^{th} frequency point of $\mathbf{H}_m$
$\overline{\mathbf{H}}_{m,i}$	i^{th} frequency point of $\overline{\mathbf{H}}_m$
i	Subscript, frequency point number
j	Subscript, data segment number for the average periodogram method
k	Total number of frames in the test
K	Specimen stiffness
K_0	Specimen initial stiffness
l	Number of input and output signals
m	Subscript, frame iteration number
M	Average time of average periodogram method
n	Number of frequency points in a frame
N	Number of points of the Fourier transform
$S_{y_{m,i}y_{m,i}}(f)$	APD of $\mathbf{S}_{y_m y_m}$ at the i^{th} frequency point
$S_{\widetilde{y}_{m,i}\widetilde{y}_{m,i}}(f)$	CPD of $\mathbf{S}_{\widetilde{y}_m\widetilde{y}_m}$ at the i^{th} frequency point
T	Time of one frame
T_{total}	Total time
$u_{m,i}$	i^{th} data point of command signal $\mathbf{u}_m$
$U_{m_j}(f)$	FFT of the j^{th} data segment of $\mathbf{u}_m$
$U^*_{m_j}(f)$	Complex conjugate of U_{m_j}
$X(s)$	Laplace transform of the input signal of a shaking table system
$y_{m,i}$	i^{th} data point of $\mathbf{y}_m$
$Y(s)$	Laplace transform of the shaking table output signal
$Y_{m_j}(f)$	FFT of the j^{th} data segment of $\mathbf{y}_m$
$\widetilde{Y}_{m_j}(f)$	FFT of the j^{th} data segment of $\widetilde{\mathbf{y}}_m$
$Y^*_{m_j}(f)$	Complex conjugate of Y_{m_j}
$\widetilde{Y}^*_{m_j}(f)$	Complex conjugate of $\widetilde{Y}_{m_j}$
Φ_{m}	Weighted sum of the m^{th} frame spectral density of the reference signal

Table A2: Vector.

$\mathbf{C}_m(f)$	m^{th} frame coherence function
$\mathbf{S}_{u_m u_m}(f)$	APD spectrum of $\mathbf{U}_m$
$\mathbf{S}_{u_m y_m}(f)$	CPD spectrum of $\mathbf{U}_m$ and $\mathbf{Y}_m$
$\mathbf{S}_{y_m y_m}(f)$	APD spectrum of $\mathbf{Y}_m$
$\mathbf{S}_{\widetilde{y}_m\widetilde{y}_m}(f)$	APD spectrum of $\widetilde{\mathbf{Y}}_m$
$\mathbf{u}_m(t)$	m^{th} frame command signal
$\mathbf{U}_m(f)$	FFT of $\mathbf{u}_m$
$\mathbf{y}_m(t)$	m^{th} frame response signal
$\widetilde{\mathbf{y}}_m(t)$	m^{th} frame reference signal
$\mathbf{Y}_m(f)$	FFT of $\mathbf{y}_m$
$\widetilde{\mathbf{Y}}_m(f)$	FFT of $\widetilde{\mathbf{y}}_m$

Table A3: Matrix.

$\mathbf{G}_m(f)$	m^{th} frame of the inverse system matrix
$\mathbf{H}(s)$	System matrix of the shaking table system
$\mathbf{H}_0(f)$	Initial system matrix
$\mathbf{H}_m(f)$	m^{th} frame identification of the system matrix
$\overline{\mathbf{H}}_m(f)$	m^{th} frame correction of the system matrix

Data Availability Statement

The data that support the findings of this study are available on request from the corresponding authors. The data are not publicly available due to privacy or ethical restrictions.

Disclosure

The opinions, findings, conclusions, and recommendations expressed in this paper are solely those of the authors and do not necessarily reflect the views of the sponsors.

Conflicts of Interest

The authors declare no conflicts of interest.

Author Contributions

Ao Xun: data curation and writing–original draft preparation. Hui-meng Zhou: conceptualization, methodology, software, and writing–review. Zhen Wang: writing–review. Fu-rong Zhang: data curation and writing–original draft preparation. Tao Wang: writing–review and investigation.

Wei-xu Song: test. David Wagg: writing–review. Shuang Zou: writing–review.

Funding

This study was supported by the National Key Research and Development Program of China, 2022YFC3801201; Natural Science Foundation of Guangdong Province, 2022A1515010500; National Natural Science Foundation of China, 51878630, 52378142; National Science Fund for Distinguished Young Scholars, 52125806; and Guangzhou City School Joint Project (2023A03J0086).

Acknowledgments

The authors express their gratitude to Engineer Wang Zhan from BBK Technology Company for his valuable advice and guidance. They also acknowledge financial support from the National Key Research and Development Project (2022YFC3801201), the Natural Science Foundation of Guangdong Province (2022A1515010500), the National Natural Science Foundation of China (51878630, 52378142), the National Science Foundation for Distinguished Young Scholars (52125806), and the Guangzhou City School Joint Project (52378142).

References

[1] J. Yao, M. Dietz, R. Xiao, H. Yu, T. Wang, and D. Yue, "An Overview of Control Schemes for Hydraulic Shaking Tables," *Journal of Vibration and Control* 22, no. 12 (2014): 2807–2823, https://doi.org/10.1177/1077546314549589.

[2] S. Günay and K. M. Mosalam, "Enhancement of Real-Time Hybrid Simulation on a Shaking Table Configuration With Implementation of an Advanced Control Method," *Earthquake Engineering & Structural Dynamics* 44, no. 5 (2014): 657–675, https://doi.org/10.1002/eqe.2477.

[3] Y. Xu, H. Hua, and J. Han, "Modeling and Controller Design of a Shaking Table in an Active Structural Control System," *Mechanical Systems and Signal Processing* 22, no. 8 (2008): 1917–1923, https://doi.org/10.1016/j.ymssp.2008.02.003.

[4] B. S. Twitchell and M. D. Symans, "Analytical Modeling, System Identification, and Tracking Performance of Uniaxial Seismic Simulators," *Journal of Engineering Mechanics* 129, no. 12 (2003): 1485–1488, https://doi.org/10.1061/(asce)0733-9399(2003)129:12(1485).

[5] N. Nakata, "Acceleration Trajectory Tracking Control for Earthquake Simulators," *Engineering Structures* 32, no. 8 (2010): 2229–2236, https://doi.org/10.1016/j.engstruct.2010.03.025.

[6] P. Pan, Y. Guo, and T. Wang, "Experimental Study of a New Kind of Double-Layer Shaking Table," *Earthquake Engineering & Structural Dynamics* 50, no. 11 (2021): 2897–2914, https://doi.org/10.1002/eqe.3478.

[7] Y. Tian, T. Wang, Y. Shi, Q. Han, and P. Pan, "Offline Iterative Control Method Using Frequency-Splitting to Drive Double-Layer Shaking Tables," *Mechanical Systems and Signal Processing* 152 (2021): 107443, https://doi.org/10.1016/j.ymssp.2020.107443.

[8] Y. Tagawa and K. Kajiwara, "Controller Development for the E-Defense Shaking Table," *Proceedings of the Institution of Mechanical Engineers-Part I: Journal of Systems & Control Engineering* 221, no. 2 (2007): 171–181, https://doi.org/10.1243/09596518jsce331.

[9] X. Ji, K. Kajiwara, T. Nagae, R. Enokida, and M. Nakashima, "A Substructure Shaking Table Test for Reproduction of Earthquake Responses of High-Rise Buildings," *Earthquake Engineering & Structural Dynamics* 38, no. 12 (2009): 1381–1399, https://doi.org/10.1002/eqe.907.

[10] G. Maddaloni, K. P. Ryu, and A. M. Reinhorn, "Simulation of Floor Response Spectra in Shake Table Experiments," *Earthquake Engineering & Structural Dynamics* 40, no. 6 (2010): 591–604, https://doi.org/10.1002/eqe.1035.

[11] H. Zhou, X. Shao, Y. Tian, et al., "Reproducing Response Spectra in Shaking Table Tests of Nonstructural Components," *Oil Dynamics and Earthquake Engineering* 127 (2019): 105835, https://doi.org/10.1016/j.soildyn.2019.105835.

[12] H. Qu, X. Huang, Y. Gao, Y. Deng, and B. Li, "HHT-based Seismic Damage Analysis of a Subgrade Slope Reinforced by a Gravity Retaining Wall," *Oil Mechanics and Foundation Engineering* 8, no. 5 (2021): 425–432, https://doi.org/10.1007/s11204-021-09761-9.

[13] A. R. Plummer, "Control Techniques for Structural Testing: A Review," *Proceedings of the Institution of Mechanical Engineers-Part I: Journal of Systems & Control Engineering* 221, no. 2 (2007): 139–169, https://doi.org/10.1243/09596518JSCE295.

[14] D. H. Owens and J. Hätönen, "Iterative Learning Control-An Optimization Paradigm," *Annual Reviews in Control* 29, no. 1 (2005): 57–70, https://doi.org/10.1016/j.arcontrol.2005.01.003.

[15] P. Chen, C. Lai, and K. Tsai, "A Control Framework for Uniaxial Shaking Tables Considering Tracking Performance and System Robustness," *Structural Control and Health Monitoring* 24, no. 11 (2017): e2015, https://doi.org/10.1002/stc.2015.

[16] S. A. Neild, D. P. Stoten, D. Drury, and D. J. Wagg, "Control Issues Relating to real-time Substructuring Experiments Using a Shaking Table," *Earthquake Engineering & Structural Dynamics* 34, no. 9 (2005): 1171–1192, https://doi.org/10.1002/eqe.473.

[17] R. Enokida and K. Kajiwara, "Nonlinear Signal-Based Control for Single-Axis Shake Tables Supporting Nonlinear Structural Systems," *Structural Control and Health Monitoring* 26, no. 9 (2019): e2376, https://doi.org/10.1002/stc.2376.

[18] J. Yao, S. Hu, W. Fu, and J. Han, "Harmonic Cancellation for electro-hydraulic Servo Shaking Table Based on LMS Adaptive Algorithm," *Journal of Vibration and Control* 17, no. 12 (2010): 1862–1868, https://doi.org/10.1177/1077546310363014.

[19] V. K. Dertimanis, H. P. Mouzakis, and I. N. Psycharis, "On the Acceleration-Based Adaptive Inverse Control of Shaking Tables," *Earthquake Engineering & Structural Dynamics* 44, no. 9 (2014): 1329–1350, https://doi.org/10.1002/eqe.2518.

[20] B. M. Phillips, N. E. Wierschem, and B. F. Spencer Jr, "Model-Based Multi-Metric Control of Uniaxial Shake Tables," *Earthquake Engineering & Structural Dynamics* 43, no. 5 (2013): 681–699, https://doi.org/10.1002/eqe.2366.

[21] B. M. Phillips and B. F. Spencer Jr, "Model-Based Feedforward-Feedback Actuator Control for Real-Time Hybrid Simulation," *Journal of Structural Engineering* 139, no. 7 (2013): 1205–1214, https://doi.org/10.1061/(asce)st.1943-541x.0000606.

[22] A. Najafi and B. F. Spencer Jr, "Modified Model-Based Control of Shake Tables for Online Acceleration Tracking," *Earthquake Engineering & Structural Dynamics* 49, no. 15 (2020): 1721–1737, https://doi.org/10.1002/eqe.3326.

[23] T. Y. Yang, K. Li, J. Y. Lin, Y. Li, and D. P. Tung, "Development of High-Performance Shake Tables Using the Hierarchical Control Strategy and Nonlinear Control Techniques," *Earthquake Engineering & Structural Dynamics* 44, no. 11 (2015): 1717–1728, https://doi.org/10.1002/eqe.2551.
[24] H. Yao, P. Tan, T. Y. Yang, and F. Zhou, "Acceleration-Based Sliding Mode Hierarchical Control Algorithm for Shake Table Tests," *Earthquake Engineering & Structural Dynamics* 50, no. 13 (2021): 3670–3691, https://doi.org/10.1002/eqe.3527.
[25] Z. Chen, T. Y. Yang, Y. Xiao, X. Pan, and W. Yang, "Model Reference Adaptive Hierarchical Control Framework for Shake Table Tests," *Earthquake Engineering & Structural Dynamics* 54 (2024): 346–362, https://doi.org/10.1007/s00603-022-02822-x.
[26] N. Rajabi, A. H. Abolmasoumi, and M. Soleymani, "Sliding Mode Trajectory Tracking Control of a Ball-Screw-Driven Shake Table Based on Online State Estimations Using EKF/UKF," *Structural Control and Health Monitoring* 25, no. 4 (2017): e2133, https://doi.org/10.1002/stc.2133.
[27] K. P. Ryu and A. M. Reinhorn, "Real-Time Control of Shake Tables for Nonlinear Hysteretic Systems," *Structural Control and Health Monitoring* 24, no. 2 (2016): e1871, https://doi.org/10.1002/stc.1871.
[28] C. Hu, R. Zhou, Z. Wang, Y. Zhu, and M. Tomizuka, "Real-Time Iterative Compensation Framework for Precision Mechatronic Motion Control Systems," *IEEE/CAA Journal of Automatica Sinica* 9, no. 07 (2022): 1218–1232, https://doi.org/10.1109/jas.2022.105689.
[29] D. Smallwood, "Multiple Shaker Random Vibration Control-An Update," *Institute of Environmental Sciences and Technology, Proceedings 1999* (1999).
[30] P. Tian and Z. Chen, "Earthquake Simulation Control of a Specimen in Elastoplastic Stage," *Journal of Vibration and Shock* 33 (2014): 43–49, (in Chinese), https://doi.org/10.13465/j.cnki.jvs.2014.18.008.
[31] F. Zhang, H. Zhou, B. Zhang, W. Song, and T. Wang, "Real-Time Iterative Control Method Research of Shaking Table," *Engineering Mechanics* 41, no. 3 (2024): 187–198, (In Chinese), https://doi.org/10.6052/j.issn.1000-4750.2022.03.0265.
[32] J. S. Bendat and A. G. Piersol, *Engineering Applications of Correlation and Spectral Analysis* (New York, NY: Wiley-Interscience Publication, 1980).
[33] Mts, "Multipurpose Testware," (2024), https://www.mtschina.com/products/software-monitoring/793mpt.
[34] S. Solutions, (2024), https://www.speedgoat.com/solutions.
[35] R. Y. Jung, *Development of real-time Hybrid Test System* (University of Colorado, 2005).
[36] Y. Tian, D. Xu, H. Zhou, and T. Wang, "Study on the TMD Damping of Wind Turbine Towers in Construction," *Engineering Mechanics* 36, no. S1 (2019): 184–188, (in Chinese), https://doi.org/10.6052/j.issn.1000-4750.2018.06.S037.
[37] Pulsar Digital Servo-controller, "Servotest-Test, Motion Simulation," (2024), https://www.servotestsystems.com/pulsar-digital-servo-controller.
[38] "SCRAMNet GT200 Fact Sheet, Curtiss-Wright Defense Solutions," (2024), https://www.curtisswrightds.com/resources/scramnet-gt200-fact-sheet.